Aus dem Institut für Biologische und Medizinische Bildgebung des Helmholtz Zentrums München

Direktor: Prof. Dr. Vasilis Ntziachristos

Automatische Segmentierung anatomischer Strukturen in CT-Bildern eines hybriden FMT/XCT-Systems zur Verbesserung der optischen Bildgebung

Dissertation
zum Erwerb des Doktorgrades der Humanbiologie
an der Medizinischen Fakultät der
Ludwig-Maximilians-Universität zu München

vorgelegt von

Marcus Freyer

aus
Bernburg

Jahr
2011

HelmholtzZentrum münchen
Deutsches Forschungszentrum für Gesundheit und Umwelt

HELMHOLTZ GEMEINSCHAFT

Berichterstatter:	Prof. Dr. Karl-Hans Englmeier
Mitberichterstatter:	Priv. Doz. Dr. Sonja M. Kirchhoff Priv. Doz. Dr. Thomas Pfluger Prof. Dr. Hartmut Brückmann
Mitbetreuung durch den promovierten Mitarbeiter:	Dr. Ralf Schulz
Dekan:	Prof. Dr. med. Dr. h.c. M. Reiser, FACR, FRCR
Tag der mündlichen Prüfung:	15. März 2011

Danksagung

Als erstes gebührt mein Dank Prof. Dr. Karl-Hans Englmeier, der mir die Möglichkeit zu dieser Promotion gab und mich auf meinem Weg immer gut betreut und unterstützt hat. Außerdem danke ich all meinen Kollegen am Helmholtz Zentrum München und dem Institut für biologische und medizinische Bildgebung für ihre fachliche Hilfe, besonders aber Harry, Peter, Thomas und Saskia sowie Chrissy, Anna-Lena, Ann-Kristin und Christine, die mit mir zusammen diesen Weg gegangen sind und denen ich nun viele, viele gute Erinnerungen an diese Zeit verdanke. Mein Dank gilt auch der Doktorandeninitiative (DINI) des Helmholtz Zentrums München und all ihren Mitgliedern für ihr Engagement zur Gestaltung der Doktorandenzeit am Zentrum.

Mein größter Dank gebührt aber meiner Freundin Anja. Du bist das Beste was mir die Zeit in München gebracht hat und das Beste in meinem Leben überhaupt.

Zusammenfassung

Die Früherkennung selbst kleinster physiologischer und funktioneller Veränderungen innerhalb eines Organismus ist gerade bei der Entwicklung neuer Medikamente von entscheidender Bedeutung. Vor allem die molekulare Fluoreszenztomografie (FMT) hat sich als äußerst hilfreich dabei erwiesen, solche Veränderungen makroskopisch und in-vivo sichtbar zu machen. Die Rekonstruktion von FMT-Bildern ist jedoch äußerst schwierig, da die Ausbreitung von Licht in biologischen Geweben durch Streuungs- und Absorptionseffekte nicht geradlinig erfolgt. Dies führt zu Fehlern und Artefakten in den FMT-Bildern. Um diese Probleme zu lösen und die Qualität der Bildgebung zu verbessern, wurde ein hybrides FMT/XCT-System konstruiert. Mit dessen Hilfe können a-priori Informationen über die Anatomie eines Versuchstieres gewonnen und für eine Verbesserung der FMT-Rekonstruktion eingesetzt werden. Dazu ist es jedoch nötig, anatomische Strukturen in den XCT-Bildern zu finden und zu klassifizieren. Ziel dieser Arbeit ist es, verschiedene Möglichkeiten aufzuzeigen, um unterschiedliche anatomische Strukturen vollautomatisch, schnell und exakt zu segmentieren. Es wird ein Framework präsentiert, welches das Skelett, die Lunge und das Herz in CT-Aufnahmen von Mäusen findet. Die Ergebnisse werden evaluiert und es wird demonstriert, wie diese Segmentierungsergebnisse in die FMT-Rekonstruktion integriert werden können und wie dadurch die Qualität von FMT-Bildern signifikant verbessert werden kann.

Abstract

The early detection of even the smallest physiological and functional changes within an organism is of critical importance especially for the development of novel pharmaceutical agents. Most notably the fluorescence molecular tomography (FMT) has proven to be helpful to visualize those changes macroscopically and in-vivo. However, the reconstruction of FMT images is very complicated because the propagation of light in biological tissues is not linear due to scattering and absorption effects. This leads to errors and artefacts within FMT images. To solve this problem and to increase imaging quality a hybrid FMT/XCT system has been developed. With its help a-priori information about the anatomy of a laboratory animal can be gained and utilized to improve FMT reconstruction. Therefore it is necessary to find and to classify anatomical structures within the XCT images. The intention of this work is to present multiple methods for the fast, automatic and accurate segmentation of anatomical structures. A framework will be presented which finds the skeleton, the lung and the heart within CT images of mice. The results are evaluated and it will be demonstrated how these segmentation results can be integrated into the FMT reconstruction and how this improves FMT image quality significantly.

Inhaltsübersicht

1. Einleitung

1.1 Einführung in die molekulare Fluoreszenztomografie

Verfahren zur dreidimensionalen biologischen und medizinischen Bildgebung wie die Röntgen-Computertomografie (engl.: X-ray Computed Tomography, XCT) oder die Magnetresonanz-tomografie (MRT) haben die moderne Medizin maßgeblich beeinflusst und verändert. Einer der Hauptgründe dafür ist ihre Fähigkeit, einen nichtinvasiven Einblick in lebende Organismen zu ermöglichen. Dadurch sind sie vor allem für die Diagnose pathologischer Veränderungen der Physiologie und Anatomie von Patienten, sowie der Beobachtung von Behandlungsfortschritten von entscheidender Bedeutung. Eine der neuesten und innovativsten Methoden der biologischen bzw. medizinischen Bildgebung stellt die Diffuse Optische Tomografie (DOT) dar, welche die Ausbreitung von Licht, d.h. von elektromagnetischer Strahlung mit einer Wellenlänge von ca. 380 bis 780 nm, in Körpern aufzeichnet, um dreidimensionale Schnittbilder zu rekonstruieren.

Da sich Licht in biologischen Geweben jedoch nicht linear ausbreitet, sondern stark durch Streuungs-, Absorptions-, und Reflektionseffekte beeinflusst wird, ist die Anatomie deutlich schwerer zu rekonstruieren als beispielsweise bei der Verwendung von Röntgenstrahlen. Die notwendigen Grundlagen zur DOT konnten deshalb erst Anfang der 90er Jahre des 20. Jahrhunderts entwickelt werden, als die ersten theoretischen Modelle zur Tomografie von diffusen Signalen veröffentlicht wurden [Arridge 1993, Graber 1993, Schotland 1992]. Wenige Jahre später wurde die DOT durch eine weitere Entwicklung in einem anderen Fachgebiet wesentlich beeinflusst: die künstlichen Herstellung des grün fluoreszierenden Proteins (GFP) [Prasher 1992, Chalfie 1994, Inouye 1994], welches in natürlicher Form in der Medusenart *Aequorea victoria* vorkommt. Dieses Protein hat die besondere Eigenschaft, Licht einer bestimmten Wellenlänge, der sogenannten Emissionswellenlänge, zu erzeugen, sobald es angeregt wird. Die Anregung erfolgt dabei ebenfalls optisch, wobei die Anregungswellenlänge nicht identisch mit der Emissionswellenlänge ist. Dadurch lässt sich die spezifische Fluoreszenz des GFP gut vom Licht der Anregungsquelle trennen. Da sich das GFP zudem praktisch beliebig mit anderen Proteinen auf genspezifische Art verbinden lässt, kann es zum Markieren von Proteinen verwendet werden.

Durch die Verwendung von GFP in der DOT entstand die Molekulare Fluoreszenztomografie (engl.: Fluorescence Molecular Tomography, FMT), die sich zu einem der vielversprechendsten Bildgebungsverfahren unserer Zeit entwickelt hat [Ntziachristos et al. 2005]. Dabei werden Fluorochrome, bei denen es sich heutzutage meist um anwendungsspezifische Variationen des originalen GFPs handelt, einem lebenden Organismus injiziert, um sich mit den anvisierten Proteinen zu verbinden. Mit Hilfe von Lasern, welche Licht der spezifischen Anregungswellenlänge der Fluorochrome ausstrahlen, können die Fluorochrome aktiviert werden und beginnen dadurch Licht ihrer spezifischen Emissionswellenlänge zu emittieren. Diese Emissionen können außerhalb des Organismus mit Hilfe von CCD-Kameras aus verschiedenen Perspektiven aufgenommen werden. Diese zweidimensionalen Bilddaten erlauben die Rekonstruktion dreidimensionaler Schnittbilder, welche die Konzentration und Verteilung der Fluorochrome, und damit des anvisierten Proteins, innerhalb des Organismus widerspiegeln.

Gerade für die medizinische Bildgebung ergeben sich durch die FMT interessante Anwendungsmöglichkeiten. So gelang es bereits Ende der 90er Jahre mit Hilfe fluoreszierender Kontrastmittel, Tumore sichtbar zu machen. Da die DOT aufgrund der geringen Eindringtiefe von Lichtwellen in organisches Gewebe bisher auf die Rekonstruktion dünner Objekte beschränkt ist, kommt sie beim Menschen nur für die oberflächliche Bildgebung in Frage. Große Bedeutung kommt ihr jedoch in der pharmazeutischen Entwicklung zu, da sie für die Untersuchung kleiner Versuchstiere wie z.B. von Mäusen sehr gut geeignet ist. Vor allem mit Licht im Nahinfrarotbereich, d.h. ab einer Wellenlänge von 650 nm, können Eindringtiefen bis zu mehreren Zentimetern erreicht werden [Chance 1991, Joebsis 1977]. Dies ist bei Kleintieren absolut ausreichend. Der Vorteil der DOT bzw. der FMT im Speziellen liegt dabei in der Möglichkeit, selbst kleinste Tumore und ihre Aktivität in-vivo, d.h. am lebenden Objekt, und makroskopisch sichtbar zu machen. Damit unterscheidet sie sich von herkömmlichen Verfahren wie XCT und MRT, in denen Tumore lediglich bei großflächigen, physiologischen Veränderungen erkannt werden können, als auch von der Mikroskopie, die zwar selbst kleinste Tumorzellen visualisieren kann, aber bei der Suche nach diesen räumlich sehr begrenzt ist. Außerdem erfordert die Mikroskopie eine invasive Biopsie, um das zu untersuchende Gewebe zu entnehmen. Die FMT eignet sich deshalb dazu, um u.a. die Wirkung pharmazeutischer Wirkstoffe auf Tumorzellen direkt und innerhalb kürzester Zeit nachzuweisen, ohne das betrachtete Versuchstier für

histologische Untersuchungen opfern zu müssen. Dadurch sind auch Studien an den selben Versuchstieren und über längere Zeiträume möglich.

Ein großes Problem der FMT ist jedoch weiterhin die Komplexität der Lichtausbreitung im Gewebe, da die Photonen sich nicht geradlinig durch ein Objekt bewegen, sondern diffus gestreut werden. Zudem kommt es auch zur teilweisen Reflexion und Absorption des Lichtes. Dies allein macht die Rekonstruktion der Fluorochromkonzentration und -verteilung bereits deutlich komplizierter als bei herkömmlichen Tomografieverfahren. Hinzu kommt, dass die unterschiedlichen Gewebearten innerhalb eines Organismus unterschiedliche Eigenschaften bezüglich der Lichtausbreitung besitzen. Daraus ergibt sich unweigerlich der Schluss, dass nur bei möglichst genauer Kenntnis der spezifischen Physiologie und Anatomie eines Organismus, eine optimale Rekonstruktion gewährleistet werden kann. Aus diesen Gründen werden für die FMT fast ausschließlich modellbasierte Rekonstruktionsverfahren angewendet.

1.2 Modellbasierte Rekonstruktion und hybride FMT-Systeme

Um das Potential der FMT auszuschöpfen, müssen die Probleme bei der Rekonstruktion gelöst werden. Eine Möglichkeit bilden modellbasierte Rekonstruktionsverfahren. Dazu wird das Rekonstruktionsproblem auf die folgende Gleichung reduziert:

$$Wx = y$$

Hierbei repräsentiert x die Fluorochromkonzentration und -verteilung innerhalb des Organismus. Die Fluoreszenzemissionen werden durch ein System bzw. Modell W beeinflusst, welches die Lichtausbreitung innerhalb des untersuchten Organismus beschreibt. Dadurch entstehen die Messwerte y d.h. die Bilddaten des FMT. Ziel einer Rekonstruktion ist es nun, x möglichst genau zu ermitteln. Da das Gleichungssystem in der Regel unterbestimmt ist, kann eine Lösung nur durch Approximation erreicht werden, d.h. es reicht, wenn das Gleichungssystem die Bedingung $Wx \approx y$ erfüllt. Eine Lösung kann dann durch Minimierung des folgenden Residuums erreicht werden:

$$\left\| Wx - y \right\|^2 \rightarrow \min$$

Wie bereits erwähnt wurde, ist die Ausbreitung des Lichts in starkem Maße von den zu durchdringenden Gewebetypen abhängig. Je nach chemischer Zusammensetzung und physischer Struktur (z.B. Oberflächenbeschaffenheit) wird Licht unterschiedlich stark absorbiert und gestreut. Wie man aus diesen Zusammenhängen erkennen kann, setzt die modellbasierte Rekonstruktion deshalb voraus, dass das Modell W möglichst akkurat an den abgebildeten Organismus angepasst wird. Ansonsten wird x zwangsläufig fehlerhaft rekonstruiert, da eine falsche Lichtausbreitung innerhalb des Gewebes angenommen wird. Es existieren zwar bereits sehr gute Methoden, um die diffuse Ausbreitung des Lichts mathematisch zu beschreiben [Arridge 1993, Flock 1989], dennoch muss immer die Heterogenität der Anatomie und Physiologie des abgebildeten Organismus berücksichtigt werden. Dies führt zu dem unweigerlichen Schluss, dass möglichst detaillierte Informationen über die spezifische Anatomie des betrachteten Organismus gewonnen werden müssen. Nur dann kann das Modell individuell auf den Organismus angepasst werden, um eine exakte Rekonstruktion der Fluorochromkonzentration und -verteilung zu ermöglichen.

Um diese Informationen zu erhalten, wurden in den letzten Jahren eine Reihe hybrider Systeme entwickelt. Dabei wird das FMT um ein zusätzliches Bildgebungssystem erweitert, welches die anatomischen Informationen liefert. Dazu eignen sich vor allem die klassischen MRT- und XCT-Geräte, da sie eine hohe Auflösung besitzen, die Anatomie gut darstellen können und sich in langjähriger Praxis bewährt haben. Am Institut für biologische und medizinische Bildgebung (engl.: Institute for Biological and Medical Imaging, IBMI) des Helmholtz Zentrums München wurde im Rahmen eines EU-Projekts die Entwicklung eines hybriden FMT/XCT-Systems vorangetrieben. Ein Ziel war es, die Qualität der optischen Bildgebung mit Hilfe anatomischer a-priori Informationen signifikant zu steigern; u.a. durch Berücksichtigung anatomischer a-priori Informationen während der Rekonstruktion. Das FMT wurde dazu in ein kommerzielles, bereits bestehendes µCT integriert.

Die wesentlichen Komponenten des XCT (Röntgenquelle und -detektor) sind in Abb. 1 auf der horizontalen Achse angebracht. Die Hauptkomponenten des FMT (Laserquelle und CCD-Kamera)

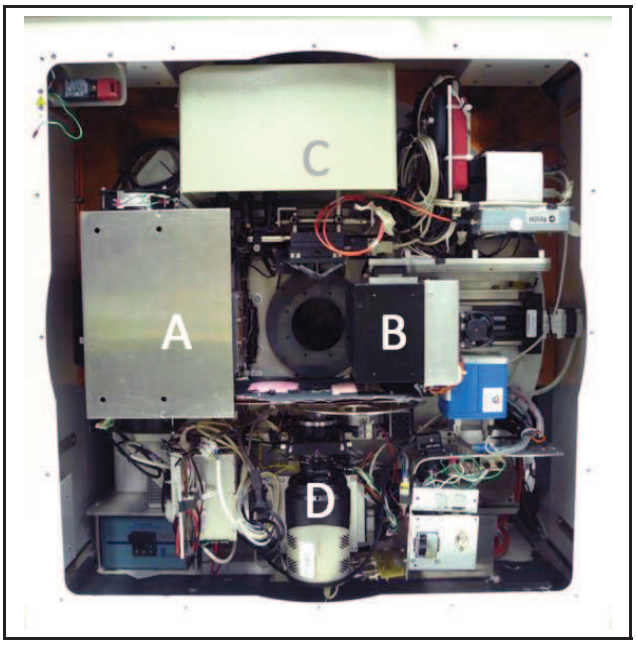

Abbildung 1: Technischer Aufbau des hybriden FMT/XCT-Systems am Institut für biologische und medizinische Bildgebung (Helmholtz Zentrum München) mit den Hauptkomponenten (A) Röntgenquelle, (B) Röntgendetektor, (C) Laser und (D) CCD-Kamera mit Filterrad.

liegen auf der vertikalen Achse. Die CCD-Kamera ist zusätzlich mit einem Filterrad ausgestattet. Dies erlaubt multispektrale Aufnahme. So können Bilder im Anregungs- und Emissionsspektrum sowie im Bereich des sichtbaren Lichts getrennt voneinander aufgenommen werden. Außerdem musste ein Bleischutz angebracht werden, um die CCD-Kamera während XCT-Aufnahmen vor den für sie schädlichen Röntgenstrahlen abzuschirmen. Die gesamte Apparatur ist auf ein bewegliches Gerüst montiert, dass 360° um das zu betrachtende Objekt rotiert werden kann.

1.3 Automatische Segmentierung zur Klassifikation anatomischer Strukturen

Es wurde beschrieben, wie mit Hilfe eines XCT anatomische Informationen gewonnen werden können, die zwangsläufig benötigt werden, um ein detailliertes Modell der Ausbreitung des Lichts innerhalb des Gewebes zu erstellen, und wie sich dadurch die Rekonstruktion der FMT verbessern lässt. Die XCT-Bilder können jedoch nicht ohne weiteres direkt verwendet werden. Der Grund dafür ist, dass keine unmittelbare Korrelation zwischen der Dichte eines Materials, d.h. seiner Intensität innerhalb der CT-Bilder, und seinen optischen Eigenschaften (im Wesentlichen Absorption und Streuung) besteht. Dies bedeutet, dass die unterschiedlichen Gewebe und Organe erst identifiziert werden müssen. Nur so ist es möglich die gewebespezifischen Parameter in das Modell zu integrieren. Da dies manuell mit einem erheblichen zeitlichen Aufwand verbunden ist, wurden Möglichkeiten gesucht, die Klassifikation anatomischer Strukturen mit Hilfe von Segmentierungsalgorithmen zu automatisieren. Dabei wurde besonderes Augenmerk auf die zeitliche Effizienz gelegt, die natürlich neben der Qualität der Klassifikation selbst, entscheidend für die praktische Anwendung ist.

Meine Aufgabe innerhalb unseres FMT/XCT-Projekts umfasste daher die komplette Entwicklung und Implementierung von Methoden zur Segmentierung anatomische Strukturen innerhalb der XCT-Bilder. Als wichtigste Strukturen wurden das Skelett, die Lunge und das Herz definiert, da das FMT/XCT vor allem für Thoraxaufnahmen verwendet werden sollte. Die wichtigsten Anforderungen an die Software waren eine hohe Qualität der Segmentierung sowie eine vollautomatische und zeiteffiziente Funktionsweise. Dadurch sollte das Programm nutzerfreundlich und die eigentliche Bildgebung nicht signifikant verlangsamt werden. Aus diesem Grund mussten größtenteils schnelle Segmentierungsmethoden zum Einsatz kommen. Zur weiteren Zeitersparnis und um das Segmentierungsergebnis zu verbessern, sollten die einzelnen Teile zudem nicht separat von einander arbeiten sondern als eine funktionelle Einheit. Dadurch würde erworbenes Wissen und Information

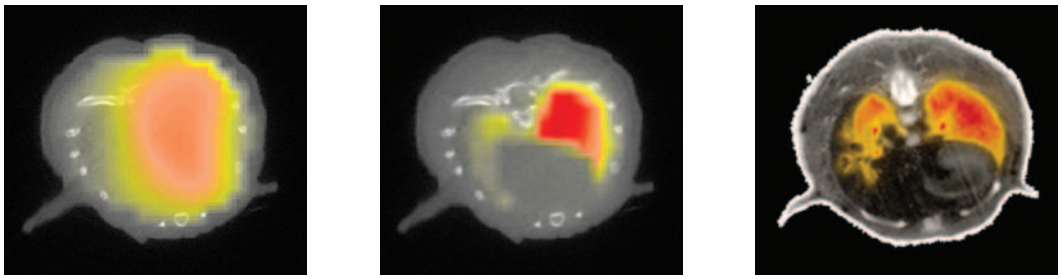

Abbildung 2: Die Bilder zeigen die Verbesserung der Rekonstruktionsqualität mit Hilfe anatomischer a-priori Informationen. Linkes Bild: Rekonstruktion ohne Berücksichtigung anatomische Informationen. Mittleres Bild: Rekonstruktion unter Berücksichtigung anatomischen Informationen. Rechtes Bild: Aufnahme der Fluoreszenz in einem Gewebeschnitt des selben Tieres zur Evaluation der Ergebnisse.

während eines Teilschrittes benutzt, um spätere Schritte beschleunigen zu können und auch die Qualität zu steigern. Die einzelnen Segmentierungen bauen deshalb immer auch auf den vorherigen Schritten und Ergebnissen auf.

Ein Beispiel dafür ist die Lungensegmentierung, bei der die ungefähre Position der Lunge mit Hilfe einer Detektion des Brustkorbs anhand des bereits segmentierten Skeletts approximiert wird. Auch die Initialposition bei der Herzdetektion basiert auf den Ergebnissen der vorherigen Schritte. Dadurch war es möglich, Zeit zu sparen und diese gewonnene Zeit in den Einsatz komplexerer Algorithmen zu investieren. Während im ersten Schritt der Software im Wesentlichen ein einfaches und schnelles Schwellwertverfahren Verwendung findet, werden im weiteren Verlauf deutlich komplexere regionenbasierte sowie modellbasierte Verfahren eingesetzt. Das bedeutet, es werden zu Beginn die einfacheren Aufgabe bewältigt, um dadurch die komplexeren besser und effizienter lösen zu können. Durch diese hierarchische Struktur können selbst aufwendigere Verfahren verwendet werden, wobei der Zeitaufwand verringert und die Segmentierungsqualität verbessert wird.

So konnte eine Software entwickelt werden, die in weniger als zwei Minuten das komplette Skelett, die Lunge sowie das Herz in Datensätzen mit etwa 3 Millionen Voxeln segmentiert. Im Vergleich zur Bilderfassung des FMT/XCT-Systems (ca. 30-60 Minuten) und der Rekonstruktion (ca. 10 Minuten) wird deutlich, dass die Segmentierung den Ablauf praktisch nicht verzögert. Zur Validierung der Segmentierungsqualität wurden die Ergebnisse des automatischen Verfahrens mit manuellen Segmentierungen verglichen. Als Maß diente der Dice-Koeffizient s der den Schnitt zweier Mengen X und Y auf Basis ihrer Gesamtgröße vergleicht:

$$s = \frac{2|X \cap Y|}{|X| + |Y|}$$

und einen Wert zwischen 0 und 1 hat, wobei 1 einer perfekten Segmentierung entspricht. Dabei konnte das von mir entwickelte Programm Dice-Werte von 0,76 bis 0,87 erreichen. Vergleicht man manuellen Segmentierungen, die von verschiedenen Personen durchgeführt wurden, ergibt sich ein Dice-Wert von etwa 0,85 bis 0,90. Dies zeigt, dass der Segmentierungsfehler zwischen Mensch und Maschine nur geringfügig größer ist als zwischen verschiedenen Menschen. Vor allem für die Verwendung in der FMT-Rekonstruktion, ist diese Qualität ausreichend.

Zusammenfassend konnte eine komplexe Programmarchitektur konstruiert werden, die durch Vollautomatisierung und Zeiteffizienz einen sehr geringen Arbeitsaufwand hat, dabei aber hilft, die Bildqualität der Fluoreszenztomografie signifikant zu verbessern. Der Vorteil ist dabei die Möglichkeit, pathologische Veränderungen wie z.B. Tumore deutlich besser und in-vivo detektieren zu können. Vor allem die visuelle Abgrenzung von Tumoren ist mit Hilfe dieses Verfahrens viel besser möglich, da Unschärfen mit dieser Methode deutlich reduziert werden konnten. Für die ersten Publikationen wurde Fluoreszenz lediglich simuliert, um die Ergebnisse korrekt gegen eine definierte Grundwahrheit validieren zu können. Mittlerweile wurden jedoch auch in-vivo Bilder verwendet und mit Hilfe von Gewebeschnitten auf ihre Richtigkeit überprüft. Diese Ergebnisse sind in Abb. 2 zu sehen. Sie zeigen am deutlichsten den Vorteil unserer Methoden. Wie man erkennen kann, ist unter Berücksichtigung der anatomischen Informationen eine sehr exakte Rekonstruktion in-vivo möglich. Um dies zu erreichen, waren die von mir entwickelten Methoden und Programme von essentieller Bedeutung.

In den beiden folgenden Publikationen wird unser FMT/XCT-Projekt detailliert vorgestellt. Dabei werden auch die Ergebnisse meiner Arbeit ausführlich dargelegt und es wird gezeigt, wie mit Hilfe der von mir entwickelten Programmarchitektur die Fluoreszenzbildgebung verbessert werden konnte. Die erste Publikation [Schulz et al. 2010] beschreibt das hybride FMT/XCT-System unserer Arbeitsgruppe sowie die grundlegende Einbindung anatomischer a-priori Information in den Rekonstruktionsprozess. Hier liegt der Fokus vor allem auf der Beschreibung der Hardware und des Rekonstruktionsansatzes. Die zweite Publikation [Freyer et al. 2010] geht speziell auf die von mir entwickelten und untersuchten Algorithmen zur Segmentierung ein, beschreibt ihr Funktionsweise und Ergebnisse und erläutert, wie diese Ergebnisse für die Rekonstruktion verwendet wurden und welche Erfolge dadurch erzielt werden konnten.

Hybrid System for Simultaneous Fluorescence and X-Ray Computed Tomography

Ralf B. Schulz*, Angelique Ale, Athanasios Sarantopoulos, Marcus Freyer, Eric Soehngen, Marta Zientkowska, and Vasilis Ntziachristos

***Abstract*—A hybrid imaging system for simultaneous fluorescence tomography and X-ray computed tomography (XCT) of small animals has been developed and presented. The system capitalizes on the imaging power of a 360°-projection free-space fluorescence tomography system, implemented within a micro-computed tomography scanner. Image acquisition is based on techniques that automatically adjust a series of imaging parameters to offer a high dynamic range dataset. Image segmentation further allows the incorporation of structural priors in the optical reconstruction problem to improve the imaging performance. The functional system characteristics are showcased, and images from a brain imaging study are shown, which are reconstructed using XCT-derived priors into the optical forward problem.**

***Index Terms*—Fluorescence tomography, hybrid imaging.**

I. Introduction

THE USE OF fluorescence in biomedical *in vivo* imaging has shown a steady increase over the past decade, as it offers a flexible platform for visualizing tissue function at the physiological, metabolical, and molecular levels in whole animals and tissues [1]. Following the successful development of fluorescent probes and reporter technologies for preclinical imaging, significant technological progress on macroscopic optical imaging has been achieved, in particular, when utilizing tomographic principles [2]–[11].

The use of hybrid methods is common in the development of imaging systems, as it offers the advantage to pack together complementary characteristics of different modalities. A most prominent example is the development of X-ray computed tomography (CT) and positron emission tomography (PET) systems for high-resolution anatomical, and high-sensitivity functional and molecular imaging, respectively [12], [13]. Hybrid methods in optical and fluorescence imaging have also been proposed in the past [14]–[16] and systems for clinical magnetic resonance imaging and optical tomography have been proposed since 1998 [17]–[22]. With the advancement of fluorescence molecular tomography (FMT) as a method to offer noninvasive tomographic reconstruction of cellular and subcellular function in tissues, it becomes similarly crucial to develop a technique for hybrid imaging that can improve imaging performance and offer a versatile imaging tool with high-dissemination potential.

Standalone FMT has undergone significant progress in terms of resolution and sensitivity. A first step in this direction was the development of free-space noncontact detection for FMT [23]–[25], which allowed to perform imaging without the use of fibers or matching fluids, by direct lens coupling of charge-coupled device (CCD) cameras, resulting in resolution and image quality improvement [26]. This development was recently taken a step further by developing systems that allow complete angle projections, around the animal or object imaged, offering 360°-projection free-space tomography [9]. Regardless, even state-of-the-art FMT systems are still far from reaching their potential of accurately visualizing biological information in high resolution for two main reasons: First, although in modern free-space systems, the reconstructed fluorescence biodistribution is registered with the outer boundaries of the imaged specimen, there is a lack of interior anatomical information to accurately orient in the tomographic image stacks. Second, the mathematical models used to date are derived using significant approximations to the photon distribution inside the volume imaged, as the interior structure of the volume is difficult to determine or remains unknown with standalone optical tomography systems.

To overcome these limitations, the combination of FMT with X-ray computed tomography (XCT) was pursued. The approach herein is markedly different than previous hybrid implementations using compromised optical collection systems, such as optical fibers inside an MR bore [22], but combines highly powerful 360°-projection free-space FMT with a high-resolution XCT system. An advantage of the development of free-space FMT is the ability to integrate it in a straightforward manner onto an XCT gantry, in transillumination mode on which a source is mounted opposite to the respective detector. XCT and FMT are truly complementary modalities. XCT offers high anatomical resolution and low soft-tissue contrast, whereas FMT offers high sensitivity and very versatile tissue contrast ability, to overall yield a hybrid system that significantly improves the information available compared to any of the components alone. With the exception of potential radiation damage to the CCD camera of the FMT system,

Manuscript received September 02, 2009; accepted October 18, 2009. First published November 10, 2009; current version published February 03, 2010. This work was supported in part by the European Union under Framework Program 7 under Grant 201792. *Asterisk indicates corresponding author.*

*R. B. Schulz is with the Chair for Biological Imaging, Technical University Munich, 80333 Munich, Germany, and also with the Institute for Biological and Medical Imaging, Helmholtz Zentrum München, German Research Center for Environmental Health, 85764 Neuherberg, Germany (e-mail: ralf.schulz@helmholtz-muenchen.de).

A. Ale, A. Sarantopoulos, M. Freyer, E. Soehngen, M. Zientkowska, and V. Ntziachristos are with the Chair for Biological Imaging, Technical University Munich, 80333 Munich, Germany, and also with the Institute for Biological and Medical Imaging, Helmholtz Zentrum München, German Research Center for Environmental Health, 85764 Neuherberg, Germany (e-mail: v.ntziachristos@tum.de).

Color versions of one or more of the figures in this paper are available online at http://ieeexplore.ieee.org.

Digital Object Identifier 10.1109/TMI.2009.2035310

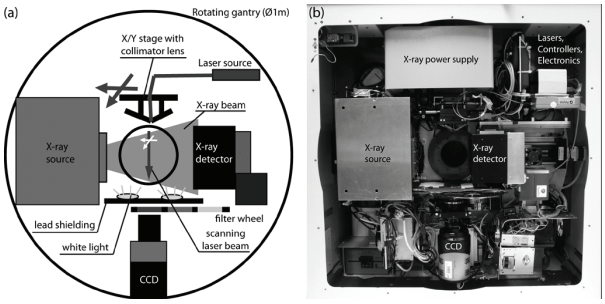

Fig. 1. Hybrid FMT/XCT imaging system. (a) Schematic top view of the rotating gantry, describing the main elements. (b) Photographic view onto the rotating gantry with front shielding and mouse bed removed. The animal is positioned in the center of the gantry.

which can be prevented using appropriate shielding, there is no interference between the optical and X-ray signals. On the other hand, XCT images provide a useful anatomical map on which FMT images overlap and can be used as a form of structural *a priori* information into the FMT reconstruction problem to improve optical imaging performance [3], [27]–[29]. While many approaches have been suggested for the use of priors, it is important to utilize methods that do not bias the result.

Herein, we present the newly developed system, and list technical and operational parameters. The performance of the developed FMT/XCT hybrid system is showcased with a brain study performed on mice. The use of priors in the forward model is investigated as a method to improve reconstruction without significantly biasing the solution.

II. Experimental Setup

A. Instrumentation

The hybrid imaging system presented herein was realized by integrating free-space FMT equipment onto the rotating gantry of a commercial micro-CT (eXplore Locus, General Electric HealthCare, London, ON, Canada). The XCT system comprises an X-ray source and an X-ray detector mounted on a common rotating gantry of ~ 1 m diameter. The distance of the X-ray detector to the center of rotation can be changed to achieve different magnification ratios, and thus, different spatial resolution. For the experiments conducted herein, a resolution of 95 μm was chosen, resulting in a field of view of ~ 35 mm along the animal and ~ 8 cm across. In the original eXplore Locus system, the animal is placed on a solid epoxy bed that can be moved along the rotating axis into the field of view of the X-ray system. The micro-CT is controlled via a standard PC (Pentium IV, 1 GB memory) and several external control units.

To integrate FMT onto the gantry, a CCD camera and a scanned laser source were mounted orthogonally to the X-ray source–detector axis, as shown in Fig. 1. A back-illuminated cooled CCD camera (Pixis 512B, Princeton Instruments, Trenton, NJ) coupled to a 50-mm macrolens (Carl Zeiss, Oberkochen, Germany) was selected for detection due to its high sensitivity. In front of the lens, a proprietary six-position filter wheel was positioned. One position in the filter wheel was occupied by a lead filter for radiation shielding during X-ray exposure, the others were different combinations of long-pass glass filters (Schott, Mainz, Germany) and bandpass filters (Andover, Salem, NH) to filter fluorescence light or the excitation wavelegth. Filter wheel and camera are located behind shielding, composed of 1 mm lead and 500 μm copper to shield the CCD from potential scattered radiation from the XCT subsystem. The field of view of the optical system covers an area of approximately 5 cm $\times$ 5 cm in the focal plane. On the opposite side of the shielding, two electroluminescent plates are mounted to provide white light illumination of the animal when needed.

Opposite to the camera along its optical axis, two collimated source fibers are mounted that can be moved by an XY stage (Standa, Vilnius, Lithuania) through the field of view of the camera. The focus length of the collimator was chosen such that the focus would be close to the animal positioned in the rotation center.

Two diode laser sources at 670 nm and 750 nm (B&W Tek, Newark, DE) with maximum optical power of 300 mW are used for illumination through the two source fibers. The laser diode modules can be selectively switched on and off, and their optical output power can be controlled via an analog input. Switching and current control is performed using a universal digital/analog input/output box with 10 bit resolution (RedLab with UBRE switchbox, Meilhaus Electronic, Puchheim, Germany). The switchbox is also used to switch on and off the white light illumination. All components for the FMT subsystem (camera, laser, D/A module, optical switch, stages) mounted on the XCT gantry are controlled through a single USB2.0 connection added to the central cable hub of the gantry and connected to a second standard PC (Pentium IV, 3 GHz, 1 GB memory). Mechanical control of the instrument and data acquisition is performed using proprietary software written in LabView (National Instruments, Austin, TX).

The mouse bed itself had to be redesigned, as the standard animal holders blocked the view. The epoxy bed was replaced by two carbon rods (Ø2 mm) 10 mm apart, mounted on two miniature linear stages (Thorlabs, Newton, NJ) to allow precise alignment of the animal to the rotation center of the gantry.

To enable simultaneous imaging without a change in the original Micro-CT framework, the communication between the motor controlling gantry rotation and the PC controlling the Micro-CT was intercepted by the FMT control PC. For details, refer to Section II-B below.

B. Data Acquisition

To start data acquisition, the user interactively defines a protocol, consisting of the angular positions at which optical imaging is to be performed, and a source pattern to be used at each angle. This source pattern is defined by the minimum and maximum axial positions, and the distance between sources in axial and transversal direction. This source pattern is adapted to the imaged object at each angular projection as described next.

Optical projection data are then acquired by rotating the gantry around the animal. At each angular position that requires measurements, the rotation is stopped and X-ray images or

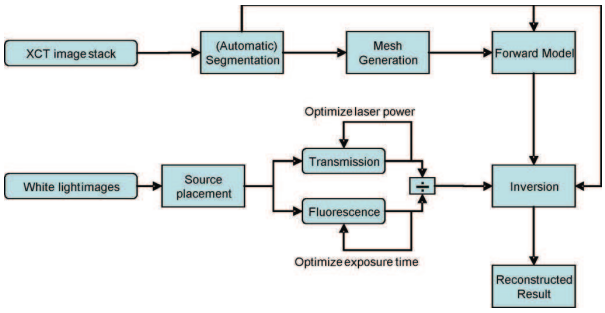

Fig. 2. Data acquisition and reconstruction scheme. XCT data, segmented into different tissue regions, is used to set up an appropriate forward model. Intrinsically coregistered FMT data, automatically optimized for optimal use of the dynamic range, is used in the inversion.

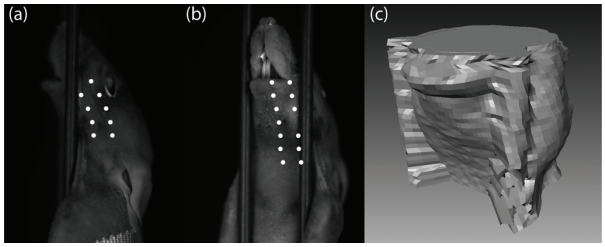

Fig. 3. Examples of acquired data. (a) and (b) White light image used to extract the boundaries of the animal for two different projection angles. The grid of source positions is automatically adapted to be centered along the animal. The resulting source positions are indicated by dots. Visible are also the black carbon rods holding the animal in place. Pixels covered by the rods are excluded from reconstruction. (c) Automatically generated finite-element mesh.

FMT images are acquired. A schematic drawing of the data acquisition procedure is shown in Fig. 2.

For XCT projections, a number of frames are acquired, and then, averaged, while the FMT system is protected using the lead filter of the filter wheel. For FMT acquisitions, first a white light image of the animal is taken, using no filter. An automatic threshold is applied to the image to distinguish between animal and background. For each row of the image, the central line of the animal is determined. The desired source pattern is then centered to this line; sources that should fall outside the animal are ignored. For all other positions, the laser is moved according to the position, and transmission and emission images are acquired, subsequently, by using different filters. Additionally, for each transmission image, the laser power is set to an optimal value by controlling the voltage on the analog input of the laser module. This laser intensity is then kept constant for the acquisition of the according fluorescence image to facilitate the accurate normalization of imaging data. However, for optimal SNR, the fluorescence exposure time is adapted. The method for optimized image acquisition is detailed in Section III-C shortly. An example of an adapted source pattern and normalized image data for a representative projection is depicted in Fig. 3(a) and (b).

Input data are extracted from the images by first considering all pixels that: 1) cover the animal, i.e., that are within the detected boundaries of the animal, and 2) reach above a certain intensity threshold in the excitation image. This way, pixels covering the rods of the animal holder, as well as very absorbing regions in the animal where no light could be detected, are excluded. The area of the remaining pixels is then covered by detector points that keep a minimum distance to each other. From these points, actual measurement values are extracted as inputs to the reconstruction.

C. Reconstruction

Photon propagation is modeled using the diffusion approximation to the radiative transport equation [7] as

$$[-\nabla D\nabla + \mu_a]\, U_m(\mathbf{r}) = -n(\mathbf{r})U_x(\mathbf{r}) \tag{1}$$

where D and μ_a are the possibly spatially varying diffusion and absorption coefficients, $n \propto c$ is some function proportional to the concentration c of fluorochrome, and U_x and U_m describe the photon density at the excitation and emission wavelength, respectively. If the (potentially spatially varying) optical coefficients are known, an explicit solution can be given using the Green's functions $G(\mathbf{r}, \mathbf{r}')$ as

$$[-\nabla D\nabla + \mu_a]\, G(\mathbf{r}, \mathbf{r}') = -\delta_0(\mathbf{r} - \mathbf{r}') \tag{2}$$

leading to

$$U_m(\mathbf{r}) = \int_{\mathbf{r}'\in \mathrm{V}} G(\mathbf{r}, \mathbf{r}')n(\mathbf{r})U_x(\mathbf{r}')\mathrm{d}\mathbf{r}'. \tag{3}$$

Equation (3) is a linear system that can be inverted using standard methods to yield n, a measure of concentration, for each voxel $\mathbf{r}'$ in volume V. For inversion, it is required to know the photon density U_x, which is usually modeled using the same Green's functions as U_m, thus assuming identical optical properties at both excitation and emission wavelength.

The Green's function are computed using a finite-element system implemented using a proprietary MATLAB interface to the Deal.II framework [30]. This system solves the diffusion equation using appropriate Robin boundary conditions, as described in the literature [31]. The necessary finite-element mesh is created from the X-ray data directly, using the outer isosurface of tissue as an outer bounday. An example of a resulting mesh is depicted in Fig. 3(c). To stabilize the solution numerically, sources and detectors are not modeled as single points, but as diffuse boundary sources of Gaussian shape with full-width half maximum (FWHM) of 1 mm, as described previously [31].

To eliminate the effect of varying source intensities and detector sensitivities in the experiments, the normalized ratio of measured fluorescence over measured transmittance U_m/U_x is used [32]. It has been shown that this normalized approach also has the capability to correct for heterogeneities of the optical coefficients [33].

Equation (3) is, by discretization, transformed into a linear system $\mathbf{Wx} = \mathbf{y}$, with $\mathbf{W}$ containing the contribution of the integral over G, $\mathbf{x}$ being the discretized vector of concentration

values n, and $\mathbf{y}$ being the vector of measurements. A stable solution to this ill-conditioned equation can be found by minimization of the regularized residual as

$$\|\mathbf{W}\mathbf{x}-\mathbf{y}\|^2+\lambda\|\mathbf{L}\mathbf{x}\|^2\rightarrow\min!. \tag{4}$$

This minimization was performed using the least-squares algorithm (LSQR) by Paige and Saunders [34]. To demonstrate the improvements obtained by hybrid versus standalone imaging, three different types of regularization matrices $\mathbf{L}$ were evaluated: 1) an identity matrix to get standard Tikhonov regularization that does not depend on structural priors; 2) a Laplace prior; and 3) a diagonal weighting prior. Both, 2) and 3) are taking into account different structures in the XCT data, as obtained through a segmentation of the volume. The most common type of regularization is Tikhonov regularization, with $\mathbf{L}=\mathbf{Id}$, leading to

$$\|\mathbf{W}\mathbf{x}-\mathbf{y}\|^2+\lambda\|\mathbf{x}\|^2\rightarrow\min!. \tag{5}$$

For optical tomography, the use of structured priors on the basis of a Laplacian regularization term has also been reported [3], [29], [35]. In this case, each voxel, i.e., each entry in $\mathbf{x}$, is assigned to a discrete region s, wher $1\leq s\leq n$. If voxels are ordered by region, $\mathbf{L}$ is a block diagonal matrix

$$\mathbf{L}=\begin{bmatrix}\mathbf{L_1} & 0 & \cdots & 0\\ 0 & \mathbf{L_2} & \ddots & \vdots\\ \vdots & \ddots & \ddots & 0\\ 0 & \cdots & 0 & \mathbf{L_n}\end{bmatrix} \tag{6}$$

where for each region s consisting of w_s voxels, and the regularizing matrix $\mathbf{L}_s$ is defined by

$$\mathbf{L_s}=\begin{bmatrix}1 & -\frac{1}{w_s} & \cdots & 0-\frac{1}{w_s}\\ -\frac{1}{w_s} & 1 & \ddots & \vdots\\ \vdots & \ddots & \ddots & -\frac{1}{w_s}\\ -\frac{1}{w_s} & \cdots & -\frac{1}{w_s} & 1\end{bmatrix}. \tag{7}$$

Each matrix element $l_{i,j}$ of the full matrix $\mathbf{L}=(l_{i,j})$ is thus given by

$$l_{i,j}=\left\{\begin{array}{cc}1, & \text{for } i=j\\ -\frac{1}{w_s}, & \text{if voxels } i \text{ and } j \text{ are in the same region } r\\ 0, & \text{otherwise}\end{array}\right\}. \tag{8}$$

The Laplace prior penalizes the variation $\nabla^2 n$ of the estimated fluorophore distribution within a region. Thus, it smoothes results within regions while allowing strong differences across region boundaries. The regions used in the reconstruction are bones, lung, heart, tumor, and other tissue.

The diagonal weighting prior is a diagonal matrix $\mathbf{L}=\operatorname{diag}\{w_i\}$ penalizing the variance of voxels i individually, depending on the region the voxels belong to. It is created in a two-step process [14], where first a piecewise constant reconstruction is performed, delivering a constant concentration value c_i for each voxel i in region r. The idea is to penalize regions with a lower value more than regions with a larger value. According the penalty w_i is set to [36]

$$w_i=\frac{(1+\beta)\max c}{(c_r+\beta)\max c}. \tag{9}$$

Parameter β is chosen arbitrarily; in this paper, we employed a value of $\beta=0.1$.

For Tikhonov regularization, the minimization of (5) can efficiently be solved for many different values of λ simultaneously using a hybrid method [37]. For the more general problem of (4), if the inverse of $\mathbf{L}$ exists, the same hybrid inversion can be used by substituting $\mathbf{x}=\mathbf{L}^{-1}\overline{\mathbf{x}}$, leading to

$$\left\|\mathbf{W}\mathbf{L}^{-1}\overline{\mathbf{x}}-\mathbf{y}\right\|^2+\lambda\|\mathbf{x}\|^2\rightarrow\min!. \tag{10}$$

The inverse of the diagonal weighting matrix is trivial to determine. Due to the block-diagonal structure of the Laplace matrix given by (6) and (7), its inverse $\mathbf{L}^{-1}=(l'_{i,j})$ can also easily be derived as

$$l'_{i,j}=\left\{\begin{array}{cc}\frac{2w_s}{w_s+1}, & \text{for } i=j \text{ and } i \text{ is in region } r\\ \frac{w_s}{w_s+1}, & \text{if voxels } i \text{ and } j \text{ are in the same region } r\\ 0, & \text{otherwise}\end{array}\right\}. \tag{11}$$

The minimization of (10) yields a result for $\overline{\mathbf{x}}$, which can then be transformed back to $\mathbf{x}$.

III. Methods and Materials

A. Geometric FMT System Calibration

After careful alignment of the optical components on the gantry, two important calibration steps need to be performed, determining: 1) the position of the rotational axis in the acquired CCD images and 2) the spatial localization of the laser beam depending on laser stage position.

The axis of rotation is found by placing a small object in the field of view of the camera and acquiring images of that object from many rotational positions. If the object is small enough and rotation symmetric, it can be assumed that its image for each angular position should look the same except for the fact that its position will change. If we assume that the optical axis of the camera is ideally parallel to the gantry plane, and that the gantry plane is orthogonal to the rotational axis, we can reduce the problem to finding the abscissa x_0 in the image that identifies the axis of rotation. The object will appear at coordinate x, following a sine curve $x=A\sin(\alpha-\varphi)$ depending on rotation angle α and the polar coordinate (A,φ) of the object, relative to the center of rotation. By determining the maximum and minimum positions $x_{\max}$ and $x_{\min}$ of the object in the image, the rotation center is determined as the mean, $x_0=1/2(x_{\min}+x_{\max})$.

Experimental determination of the rotation center was performed by imaging a 25 G injection needle (Ø0.5 mm, length 24 mm) placed in the field of view. The needle was painted black, and imaged against a white background [see Fig. 4(a)]. A region of interest was chosen interactively in which only the needle was visible. From this region, the horizontal position

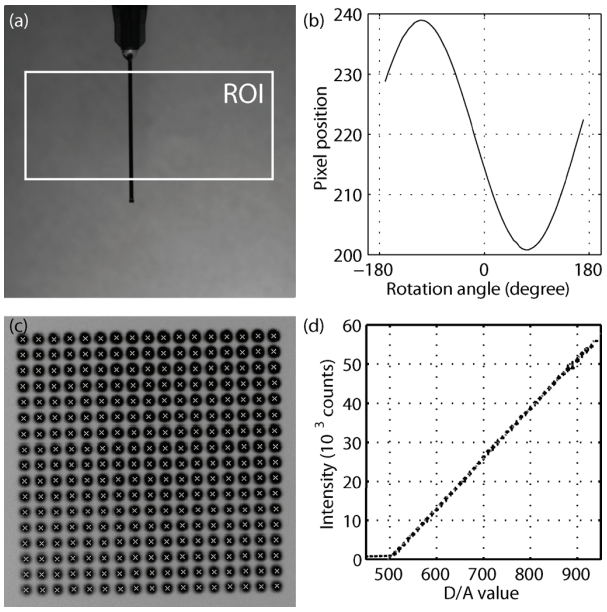

Fig. 4. System calibration procedure. Determination of the rotation center in CCD images is performed by (a) acquiring images of a needle placed in the field of view at different rotation angles and (b) extracting the sinusoidal movement whose center is at the rotation center. (c) Inverted grayscale image of the laser source, moving on a grid with 1.5 mm distance. White crosses show the predicted positions. (d) Linearity measurement of the laser intensity, as obtained in ten independent measurements.

of the needle was extracted at different angular positions [see Fig. 4(b)]. The center between the two maxima defines the coordinate of the rotation center. This experiment was repeated several times with the object placed at different positions in space. The accuracy of the measurement was ± 0.5 pixel.

For laser stage calibration, the laser spot as created on a sheet of paper placed on the animal bed was imaged, while moving both stages on a fixed grid pattern with 1.5 mm distance [see Fig. 4(c)]. The change in image position of the resulting spots for movements along the two linear stages was used to determine 2-D vectors on the image along which each individual axis moves.

B. Coregistration of FMT and XCT Data

While both subsystems, XCT and FMT, are mounted on a common geometrical arrangement, an initial calibration to match both individual coordinate systems is necessary.

The XCT was factory-calibrated to deliver X-ray volumes matched to a metric coordinate system centered to the axis of rotation and the center of the X-ray source path, with the coordinate axes aligned to the rotational, horizontal, and vertical axes. After calibration of the FMT subsystem, as described previously, resulting datasets are automatically delivered in a coordinate system centered to the axis of rotation and having a defined vertical axis. The only remaining unknown is the axial distance between optical axis and X-ray source. To determine this value, a small piece of metal wire (Ø0.5 mm) placed on black paper on the animal bed was imaged in a vertical X-ray projection, as well as optically. The shift between both images was subsequently evaluated, determining the axial offset to be 5.0 mm.

C. Optimization of Excitation and Fluorescence Acquisitions

Each pair of excitation (transmission) and fluorescence images for a single source position is optimized by using the maximum laser power for the acquisition of excitation images that does not saturate the images, and subsequently, adapting the exposure time for fluorescence images. Images are considered to be optimal if the maximum intensity $I_{\max}$ is above a given threshold I_{thresh}, but below the saturation point I_{sat}, which we set to 90% of the theoretical maximum intensity deliverable by the CCD.

Optimal transmission images are acquired in an iterative manner as follows.

1) Acquire an image using low laser power at voltage $V_{\min}$. This image has a maximum intensity $I_{\max}$.
2) Select a new voltage $V = c_V\,(I_{\text{thresh}}/I_{\max})\,V_{\min}$, where c_V is a proportionality constant relating voltage to detected intensities.
3) Repeat as necessary, or stop after a maximum of three iterations.

The coefficient c_V was experimentally determined by transilluminating a thick object of scattering and absorbing material, and detecting the voltage-dependant mean intensity $\overline{I}(V)$ over a chosen region of interest, to which a linear regression line $\overline{I}(V) = c_V V + V_0$ was subsequently fit [see Fig. 4(d)]. The coefficient c_{v} is independent of the detection method or types of filters used, exposure time, and optical properties of the phantom.

Subsequent fluorescence image acquisition is optimized by keeping the voltage constan,t but summing a number of acquired frames using a constant exposure time until the threshold was reached or a maximum total exposure of 10 s was reached. The mean read noise was automatically subtracted from each individual frame prior to the summation.

D. Creation and Imaging of Artificial Brain Lesion

In the brain of euthanized nude mice, a mixture of 1 μMol/l Alexa 750 fluorochrome and clinical CT contrast agent were stereotactically implanted at a depth of 4 mm in the right brain lobe. The animal was then placed in the imaging machine with its ears taped to the back to prevent imaging artifacts.

Reconstructed XCT data were then automatically segmented into bones and tissue by applying an automatically estimated threshold for the bones. Due to the high concentration of clinical contrast agent in the brain lesion, this segment was automatically detected as bone. In a manual step, the lesion was separated from the automatically segmented bone to create a new segment. The result of the segmentation can be seen in Fig. 6(a) and (b).

IV. Experimental Results

From 18 projections with 2×7 sources each, a total of $\sim$12000 source–detector pairs were utilized. Voxel resolution for reconstruction was 1 mm, yielding a total of 1700 voxels inside the mesh. For inversion, 100 LSQR iterations were used, simultaneously obtaining results for 200 different values of the regularization parameter λ, distributed on a logarithmic

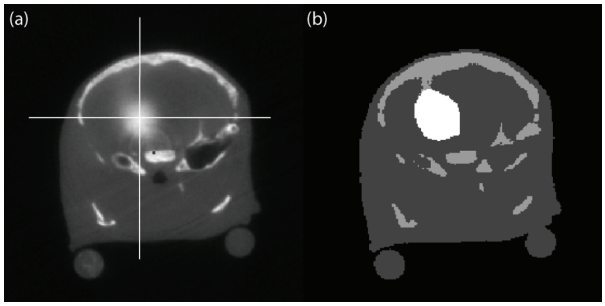

Fig. 5. (a) XCT slice showing the artificial brain lesion due to the injected CT contrast agent. The profiles in Fig. 7 are taken from the two cross sections indicated by white lines. (b) Segmentation of XCT slice into tissue (dark gray), bones (light gray), and lesion (white).

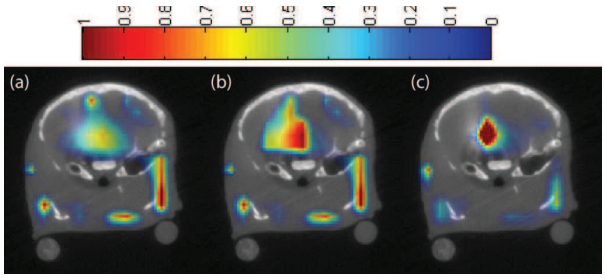

Fig. 6. Reconstructed slices on an arbitrary color scale. Reconstructions used are (a) Tikhonov regularization, (b) Laplace regularization, and (c) weighted-segment diagonal regularization.

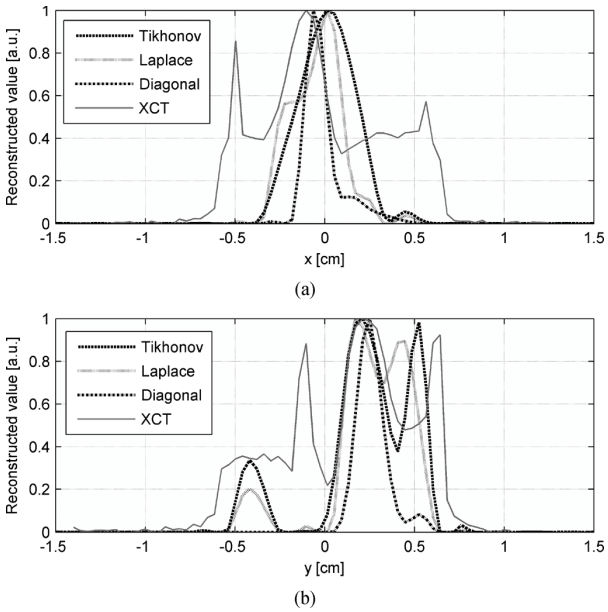

Fig. 7. Intensity profiles taken through the volume slices shown in Fig. 5, alongside with XCT intensity profile at the same position. (a) Profiles along the x-axis. (b) Profiles along the y-axis.

scale. From these results, the optimal value of λ was chosen by determining the position of the L-corner. Experimental measurements were acquired in approximately 1 h although much faster acquisitions can be reached with system optimization. Constructing the mesh and weight matrix (forward problem) required ~ 10 min on a standard PC (Intel CoreDuo processor, 2 GB RAM), using a hexahedral finite-element grid with $> 60\,000$ first-order elements. Weight matrix inversion was performed in < 1 min.

XCT is capable of visualizing the injected bolus clearly, as can be seen from the central XCT volume slice shown in Fig. 5(a). The according semiautomatic segmentation is depicted in Fig. 5(b), separating tissue, bones, and lesion.

All three inversion methods succeed in resolving the lesion with a spatial accuracy corresponding to voxel resolution (1 mm). Reconstructed FMT slices at the same position as the X-ray reconstruction in Fig. 5 are presented in Fig. 6, overlaid onto the X-ray slice. Reconstructed values are given on an arbitrary scale, normalized for each image. Due to the fact that regularization matrices change absolute reconstructed values in an, up to now, unknown fashion, we did not attempt to deliver absolutely quantitative results. Instead, we perform a relative comparison between the images, each created with an optimal lambda chosen with respect to the image quality.

Tikhonov regularization [see Fig. 6(a)] delivers the worst contrast between signal from the lesion and artifacts than Laplace regularization [see Fig. 6(b)] or the two-step diagonal weighting method [see Fig. 6(c)]. In fact, the artifacts appear at least two times stronger than the lesion, while in the Laplace method, artifacts and lesion are of the same order of magnitude. Using diagonal weighting, the amplitude of artifacts is at most 20% of the maximum reconstructed value inside the lesion.

Fig. 7 shows two profile plots through the shown reconstructed slice along the x- and y-axis, at the position depicted in Fig. 5(a). Additionally, the profile of the XCT slice is provided. The lesion on the XCT image has a fFWHM of 2.1 mm along x, corresponding to only 2–3 voxels in FMT, and 2.5 mm along y. The respective reconstructed FWHMs are 4/2.5 mm (x, y for Tikhonov regularization), 3.5/4.2 mm (x, y for Laplace regularization), and 1.4/1.8 mm (x, y for diagonal weighting). FWHMs were determined on a cubic interpolation of reconstructed voxel values to reach submillimeter estimations.

Regarding artifacts in the profiles, in the profile along y, a strong second peak appears on the right side of the inclusion with an amplitude similar to the inclusion for Tikhonov regularization and smaller amplitude for the Laplace method. It nearly disappears when using the weighted diagonal regularizer. Interestingly enough, this artifact for the Laplace method is moving closer toward the reconstructed lesion and obscuring this main peak, leading to the lower spatial resolution (FWHM) as stated previously. A reason for this bad performance of the Laplace method is that for the construction of the regularization matrix as described further previously, each voxel is just attributed to one single segment. As the actual lesion is very small, we chose to consider every voxel that is at least 10% inside the lesion segment to be part of that lesion. As the Laplace method smoothes over whole segments, this overestimation of segment size will also lead to a blurring in the result, lowering achievable resolution. This drawback is not present for the weighted diagonal method.

The small underestimation of lesion size in the weighted diagonal method can possibly be attributed to partial volume effects due to the small lesion size with respect to voxel resolution. The same holds for the shift that can be observed between the lesion center on the XCT image and in reconstructed images. Along x, the locational error in the Tikhonov and Laplace result is ~ 1 mm (corresponding to a single voxel), while for the weighted diagonal method, it is reduced to ~ 0.2 mm (0 voxels). Along y, in all methods, the locational accuracy is fully reached (< 0.5 mm error).

V. Discussion

Herein, we presented a hybrid system for combined XCT and free-space 360° FMT. This is the first system developed to offer a fully integrated FMT and XCT components delivering intrinsically coregistered datasets. The system dynamically adjusts acquisition parameters to achieve high dynamic range and employs semiautomatic segmentations of the XCT stacks to be used as structural priors in the reconstruction. By utilizing priors to improve the forward problem, experimental results show the benefits of the hybrid approach over standalone implementation, in particular, the accurate superposition of molecular contrast onto anatomical images and the delivery of improved FMT performance.

Obviously, much more work needs to be done with respect to defining an optimal regularization method. The three methods used herein were used as standard examples for regularized inversion, but have never been compared in detail. However, even without having a gold standard for hybrid reconstruction, we could show that the inclusion of *a priori* information in a Laplace or weighted diagonal matrix significantly improves SNR; resolution and spatial accuracy, however, were only significantly improved for the two-step diagonal weighting method.

The combination of FMT and XCT in one system offer highly complementary characteristics that can lead to practical systems of high-dissemination potential. The image contrast employed in orthogonal, i.e., each of the two modalities collects markedly different information on the object under investigation. Standalone XCT has significant limitations as to the tissue contrast it can achieve and its low sensitivity in molecular imaging applications. Conversely, FMT is one of the most versatile methods in terms of molecular imaging contrast, but lacks anatomical information and resolution. The combination of the two, yields a modality that not only combines information on tissue contrast, but one with the potential to improve FMT performance through the use of priors, leading overall to a truly novel implementation with superior imaging characteristics, compared to XCT and FMT operating as standalone.

While several methods for the use of *a priori* information have been suggested, it is important to select methods that do not bias the solution. For this reason, herein, we employed a moderate use of image priors, with no assumptions on the fluorescence biodistribution and demonstrate that even simple approaches like the one presented bear strong potential to improve the inversion capacity over standalone approaches that need to significantly regularize the inversion problem and reduce the resolution offered in order to yield high-fidelity imaging. A truly hybrid system, such as the FMT-XCT developed herein, further allows the collection of datasets that can lead to accurate evaluation of different algorithms using priors. Therefore, the current availability of such system points to further validation or new development of algorithms for optimal use of priors.

TABLE I
Acquisition Times

Action	Required Time
X-ray imaging[a]	0:05h
Optical acquisitions[b]	0:10h
Gantry movement	0:11h
Movement of laser and filter wheel, software overhead[c]	0:34h
Total acquisition time	**1:00h**

[a]The protocol used an angular stepping of 0.9° for full 360°, resulting in 400 angular positions. At each position, the resulting image was averaged over two frames acquired with 400 ms exposure each.

[b]The FMT acquisitions were performed every 20° over full 360°, resulting in 18 angular positions. At each position, one white light image (100 ms exposure) and 14 source positions were acquired, resulting in a total of 252 sources from which 184 were used in the reconstruction. At each source position, up to three transmission images (300 ms exposure) and up to ten emission images (1s exposure each) were acquired, depending on received light intensities.

[c]The time was estimated by subtracting the total exposures of the FMT acquisition (0:10h, as obtained from the log files), and the total duration of the XCT protocol (0:16h) from the total acquisition time (1:00h). The stated time includes the data transfer between CCD and PC and movement of mechanical parts.

The required experimental times for the presented prototype are in the order of 1 h, which limits throughout and applications in imaging of fast-changing phenomena. However, the acquisition time achieved is a result of a system unoptimized for speed, at each current state. With faster stages and gantries, as well as the interleaving of acquisition of XCT and FMT data, it is expected that future acquisition times can become of the order of 10–15 min or better (see Table I).

Further imaging improvements can be obtained by the use of an inhomogeneous forward model, taking into account the differences in attenuation and scattering coefficients between tissue types, preferably as found in the XCT data. However, as opposed to optoacoustic tomography, where results can directly be interpreted as optical attenuation coefficients [38], which allows for easy integration into hybrid optoacoustic/fluorescence tomography systems [39], optical attenuation coefficients and XCT densities are unrelated. A preferable approximation would be the use of segmentations as derived from the XCT and the extraction of average tissue properties as published for example by Niedre [40]. This method has shown certain improvements in simulation studies [41].

The results presented herein relied on relatively large, coarse segmentations that required limited user interaction. Future research should incorporate fully automatic reliable segmentations, as can be for example obtained using anatomic atlases [42] to lead to a fully automated system.

Overall, we have showcased the development and improved ability of an FMT-XCT system. The system can be built of relative low-cost components and at small form factors, thus leading to high dissemination of this technology for biomedical research and drug discovery applications.

ACKNOWLEDGMENT

We acknowledge the helpful support of P. Picot from GE Helthcare, London, ON, Canada, and fruitful discussions with D. Regulla from Helmholtz Center Munich, as well as W. Stiller from the German Cancer Research Center (dkfz), Heidelberg, Germany, regarding radiation safety and CCD protection.

REFERENCES

[1] V. Ntziachristos, J. Ripoll, L. H. V. Wang, and R. Weissleder, "Looking and listening to light: The evolution of whole-body photonic imaging," *Nat. Biotechnol.*, vol. 23, pp. 313–320, 2005.

[2] V. A. Markel and J. C. Schotland, "On the convergence of the Born series in optical tomography with diffuse light," *Inverse Problems*, vol. 23, pp. 1445–1465, 2007.

[3] S. C. Davis, H. Dehghani, J. Wang, S. Jiang, B. W. Pogue, and K. D. Paulsen, "Image-guided diffuse optical fluorescence tomography implemented with Laplacian-type regularization," *Opt. Exp.*, vol. 15, pp. 4066–4082, 2007.

[4] S. Srinivasan, B. W. Pogue, H. Dehghani, F. Leblond, and X. Intes, "Data subset algorithm for computationally efficient reconstruction of 3-D spectral imaging in diffuse optical tomography," *Opt. Exp.*, vol. 14, pp. 5394–5410, 2006.

[5] A. Corlu, R. Choe, T. Durduran, M. A. Rosen, M. Schweiger, S. R. Arridge, M. D. Schnall, and A. G. Yodh, "Three-dimensional in vivo fluorescence diffuse optical tomography of breast cancer in humans," *Opt. Exp.*, vol. 15, pp. 6696–6716, 2007.

[6] M. Schweiger, S. R. Arridge, O. Dorn, A. Zacharopoulos, and V. Kolehmainen, "Reconstructing absorption and diffusion shape profiles in optical tomography by a level set technique," *Opt. Lett.*, vol. 31, pp. 471–473, 2006.

[7] S. R. Arridge, "Optical tomography in medical imaging," *Inverse Probl.*, vol. 15, pp. R41–R93, 1999.

[8] M. D. McCluskey, L. Hsu, L. Wang, and E. E. Haller, "Infrared absorption of solid nitrogen at high pressures," *Phys. Rev. B*, vol. 54, pp. 8962–8964, 1996.

[9] N. Deliolanis, T. Lasser, D. Hyde, A. Soubret, J. Ripoll, and V. Ntziachristos, "Free-space fluorescence molecular tomography utilizing 360 degrees geometry projections," *Opt. Lett.*, vol. 32, pp. 382–384, 2007.

[10] V. A. Markel and J. C. Schotland, "Multiple projection optical diffusion tomography with plane wave illumination," *Phys. Med. Biol.*, vol. 50, pp. 2351–2364, 2005.

[11] V. A. Markel and J. C. Schotland, "Symmetries, inversion formulas, and image reconstruction for optical tomography," *Phys. Rev. E*, vol. 70, pp. 056616-1–056616-19, 2004.

[12] M. E. Phelps, *PET: Molecular Imaging and its Biological Applications*. New York: Springer-Verlag, 2004.

[13] G. K. v. Schulthess, *Clinical Molecular Anatomic Imaging: PET, PET/CT, and SPECT/CT*. Philadelphia, PA: Lippincott, 2003.

[14] D. Hyde, R. DeKleine, S. A. MacLaurin, E. Miller, E. Miller, D. H. Brooks, T. Krucker, and V. Ntziachristos, "Hybrid FMT-CT imaging of amyloid-[beta] plaques in a murine Alzheimer's disease model," *Neuroimage*, vol. 44, pp. 1304–1311, 2009.

[15] S. Srinivasan, B. W. Pogue, C. Carpenter, S. Jiang, W. A. Wells, S. P. Poplack, P. A. Kaufman, and K. D. Paulsen, "Developments in quantitative oxygen-saturation imaging of breast tissue in vivo using multispectral near-infrared tomography," *Antioxidants Redox Signal.*, vol. 9, pp. 1143–1156, 2007.

[16] B. W. Pogue, H. Q. Zhu, C. Nwaigwe, T. O. McBride, U. L. Osterberg, K. D. Paulsen, and J. F. Dunn, "Hemoglobin imaging with hybrid magnetic resonance and near-infrared diffuse tomography," in *Oxygen Transport to Tissue Xxiv*. New York: Springer, 2003, vol. 530, pp. 215–224.

[17] V. Ntziachristos, X. H. Ma, and B. Chance, "Time-correlated single photon counting imager for simultaneous magnetic resonance and near-infrared mammography," *Rev. Sci. Instrum.*, vol. 69, pp. 4221–4233, 1998.

[18] Y. Lin, H. Gao, O. Nalcioglu, and G. Gulsen, "Fluorescence diffuse optical tomography with functional and anatomical a priori information: Feasibility study," *Phys. Med. Biol.*, vol. 52, pp. 5569–5585, 2007.

[19] B. J. Tromberg, B. W. Pogue, K. D. Paulsen, A. G. Yodh, D. A. Boas, and A. E. Cerussi, "Assessing the future of diffuse optical imaging technologies for breast cancer management," *Med. Phys.*, vol. 35, pp. 2443–2451, 2008.

[20] S. C. Davis, B. W. Pogue, R. Springett, C. Leussler, P. Mazurkewitz, S. B. Tuttle, S. L. Gibbs-Strauss, S. S. Jiang, H. Dehghani, and K. D. Paulsen, "Magnetic resonance-coupled fluorescence tomography scanner for molecular imaging of tissue," *Rev. Sci. Instrum.*, vol. 79, pp. 064302-1–064302-10, 2008.

[21] C. M. Carpenter, B. W. Pogue, S. D. Jiang, H. Dehghani, X. Wang, K. D. Paulsen, W. A. Wells, J. Forero, C. Kogel, J. B. Weaver, and S. P. Poplack, "Image-guided optical spectroscopy provides molecular-specific information in vivo: MRI-guided spectroscopy of breast cancer hemoglobin, water, and scatterer size," *Opt. Lett.*, vol. 32, pp. 933–935, 2007.

[22] V. Ntziachristos, A. G. Yodh, M. Schnall, and B. Chance, "Concurrent MRI and diffuse optical tomography of breast after indocyanine Green enhancement," *Proc. Nat. Acad. Sci. USA*, vol. 97, pp. 2767–2772, 2000.

[23] R. B. Schulz, J. Ripoll, and V. Ntziachristos, "Experimental fluorescence tomography of tissues with noncontact measurements," *IEEE Trans. Med. Imag.*, vol. 23, no. 4, pp. 492–500, Apr. 2004.

[24] R. B. Schulz, J. Ripoll, and V. Ntziachristos, "Noncontact optical tomography of turbid media," *Opt. Lett.*, vol. 28, pp. 1701–1703, 2003.

[25] J. Ripoll, R. B. Schulz, and V. Ntziachristos, "Free-space propagation of diffuse light: Theory and experiments," *Phys. Rev. Lett.*, vol. 91, pp. 103901-1–103901-4, 2003.

[26] R. B. Schulz, J. Peter, W. Semmler, C. D'Andrea, G. Valentini, and R. Cubeddu, "Comparison of noncontact and fiber-based fluorescence-mediated tomography," *Opt. Lett.*, vol. 31, pp. 769–771, 2006.

[27] P. K. Yalavarthy, B. W. Pogue, H. Dehghani, C. M. Carpenter, S. D. Jiang, and K. D. Paulsen, "Structural information within regularization matrices improves near infrared diffuse optical tomography," *Opt. Exp.*, vol. 15, pp. 8043–8058, 2007.

[28] A. Li, G. Boverman, Y. H. Zhang, D. Brooks, E. L. Miller, M. E. Kilmer, Q. Zhang, E. M. C. Hillman, and D. A. Boas, "Optimal linear inverse solution with multiple priors in diffuse optical tomography," *Appl. Opt.*, vol. 44, pp. 1948–1956, 2005.

[29] M. Guven, B. Yazici, X. Intes, and B. Chance, "Diffuse optical tomography with a priori anatomical information," *Phys. Med. Biol.*, vol. 50, pp. 2837–2858, 2005.

[30] W. Bangerth, R. Hartmann, and G. Kanschat, "Deal.II—A general-purpose object-oriented finite element library," *ACM Trans. Math. Softw.*, vol. 33, pp. 24.1–24.27, 2007.

[31] M. Schweiger, S. R. Arridge, M. Hiraoka, and D. T. Delpy, "The finite-element method for the propagation of light in scattering media—Boundary and source conditions," *Med. Phys.*, vol. 22, pp. 1779–1792, 1995.

[32] V. Ntziachristos and R. Weissleder, "Experimental three-dimensional fluorescence reconstruction of diffuse media by use of a normalized Born approximation," *Opt. Lett.*, vol. 26, pp. 893–895, 2001.

[33] A. Soubret, J. Ripoll, and V. Ntziachristos, "Accuracy of fluorescent tomography in the presence of heterogeneities: Study of the normalized born ratio," *IEEE Trans. Med. Imag.*, vol. 24, no. 10, pp. 1377–1386, Oct. 2005.

[34] C. C. Paige and M. A. Saunders, "LSQR: An algorithm for sparse linear equations and sparse least squares," *ACM Trans. Math. Softw.*, vol. 8, pp. 43–71, 1982.

[35] X. Intes, C. Maloux, M. Guven, B. Yazici, and B. Chance, "Diffuse optical tomography with physiological and spatial a priori constraints," *Phys. Med. Biol.*, vol. 49, pp. N155–N163, 2004.

[36] D. Hyde, E. Miller, D. H. Brooks, and V. Ntziachristos, "New techniques for data fusion in multimodal FMT-CT imaging," in *5th IEEE Int. Symp. Biomed. Imag.: From Nano to Macro*, Paris, France, 2008.

[37] M. Hanke and P. C. Hansen, "Regularization methods for large-scale problems," *Surv. Math. Ind.*, vol. 3, pp. 253–315, 1993.

[38] Z. Yuan, Q. Z. Zhang, and H. B. Jiang, "Simultaneous reconstruction of acoustic and optical properties of heterogeneous media by quantitative photoacoustic tomography," *Opt. Exp.*, vol. 14, pp. 6749–6754, 2006.

[39] D. Razansky and V. Ntziachristos, "Hybrid photoacoustic fluorescence molecular tomography using finite-element-based inversion," *Med. Phys.*, vol. 34, pp. 4293–4301, 2007.

[40] M. J. Niedre, G. M. Turner, and V. Ntziachristos, "Time-resolved imaging of optical coefficients through murine chest cavities," *J. Biomed. Opt.*, vol. 11, pp. 064017-1–064017-7, 2006.

[41] D. Hyde, R. B. Schulz, E. Miller, D. Brooks, and V. Ntziachristos, "Performance dependence of hybrid X-ray CT–FMT on the optical forward problem," *J. Opt. Soc. Amer. A, Opt. Image Sci. Vis.*, vol. 26, pp. 919–923, 2009.

[42] M. Baiker, J. Dijkstra, I. Que, C. W. G. M. Lowik, J. H. C. Reiber, and B. P. F. Lelieveldt, "Organ approximation in muCT data with low soft tissue contrast using an articulated whole-body atlas," in *Proc. IEEE Int. Symp. Biomed.Imag.: From Nano to Macro*, Paris, France, 2008, pp. 1267–1270.

Journal of Biomedical Optics 15(3), 036006 (May/June 2010)

Fast automatic segmentation of anatomical structures in x-ray computed tomography images to improve fluorescence molecular tomography reconstruction

Marcus Freyer
Angelique Ale
Ralf B. Schulz
Technical University Munich
Biological Imaging
Munich, Germany
and
Helmholtz Zentrum München
Institute for Biological and Medical Imaging
1 Ingolstädter Landstraße
Neuherberg, 85764 Germany

Marta Zientkowska
Helmholtz Zentrum München
Institute of Stem Cell Research
1 Ingolstädter Landstraße
Neuherberg, 85764 Germany

Vasilis Ntziachristos
Karl-Hans Englmeier
Technical University Munich
Biological Imaging
Munich, Germany
and
Helmholtz Zentrum München
Institute for Biological and Medical Imaging
1 Ingolstädter Landstraße
Neuherberg, 85764 Germany

Abstract. The recent development of hybrid imaging scanners that integrate fluorescence molecular tomography (FMT) and x-ray computed tomography (XCT) allows the utilization of x-ray information as image priors for improving optical tomography reconstruction. To fully capitalize on this capacity, we consider a framework for the automatic and fast detection of different anatomic structures in murine XCT images. To accurately differentiate between different structures such as bone, lung, and heart, a combination of image processing steps including thresholding, seed growing, and signal detection are found to offer optimal segmentation performance. The algorithm and its utilization in an inverse FMT scheme that uses priors is demonstrated on mouse images.
[DOI: 10.1117/1.3431101]

Keywords: automatic image segmentation; x-ray computed tomography; fluorescence molecular tomography; Laplace regularized reconstruction.

Paper 10066R received Feb. 9, 2010; revised manuscript received Mar. 16, 2010; accepted for publication Mar. 16, 2010; published online Jun. 1, 2010.

1 Introduction

Optical tomography has drawn significant attention in recent years due to its operational simplicity and the rich contrast offered, especially when employing targeted fluorochromes. Fluorescence molecular tomography (FMT) in particular has been shown to be capable of resolving highly versatile cellular and subcellular contrast in whole animals[1,2] *in vivo* and noninvasively. There have been significant technological developments in FMT methods, especially associated with 360-deg projection free-space techniques that avoid the use of matching fluids,[3–6] the use of charge-coupled device (CCD) cameras for high spatial sampling of data fields,[7] and the development of fast and tomographic algorithms to impart quantitative 3-D imaging.[8–12] In addition, the use of early photons has further shown imaging improvements over constant intensity illumination data. These developments essentially bring out the full potential of stand-alone diffuse optical tomography methods.

The use of image priors has been also considered for further improving the performance of the optical tomography reconstruction over stand-alone systems.[13–17] A common approach is the utilization of anatomical information for the construction of a more accurate solution to the forward problem, or the regularization of the ill-posed inverse problem, resulting in improved image fidelity and resolution. To capitalize on the improvements that are offered by the use of image priors, there has been recent interest in the development of hybrid imaging systems.[18–24] Our group has recently developed a fully integrated FMT x-ray computed tomography (XCT) scanner, where all optical and CT components are mounted on a common gantry.[25] This modality provides accurately registered CT data that can be used to improve FMT image quality. A particular requirement that in consequence arose is the segmentation of the CT data to identify different organs or structures in the tissue imaged. This is important for three main reasons. The identification of different structures and their corresponding interfaces allows the generation of more accurate numerical meshes for the optical tomography problem. Importantly, they also allow for the assignment of optical properties, based on the knowledge of the optical properties of the organ or structure segmented, since there is no direct relation between x-ray CT images and optical attenuation. Finally, the resolved structures can then be used to

Address all correspondence to: Marcus Freyer, Helmholtz Zentrum München, Institute for Biological and Medical Imaging, 1 Ingolstädter Landstraße, Neuherberg, 85764 Germany. Tel: 49-(0)-89-3187-3885; Fax: 49-(0)-3187-3017; E-mail: marcus.freyer@helmholtz-muenchen.de

1083-3668/2010/15(3)/036006/8/$25.00 © 2010 SPIE

guide the inversion scheme utilized, as further explained in the methods.

We therefore considered an automatic segmentation scheme for streamlining the FMT-XCT inversion. Several approaches have been suggested in the past for automated segmentation of medical CT images.[26–30] However, the segmentation and subsequent utilization of the results into the FMT-XCT code required different image processing approaches compared to published methods for medical CT data. The differences can be attributed related to the use of μCT data, i.e., data of varying noise levels and reduced image contrast between organs compared to clinical CT data.

In addition, the work here considers an automatic integration scheme of segmented data into the FMT inversion scheme. Particular attention has been given to obtaining efficient computation to reach fast inversion times. For this reason, attention was given to the use of low dimensional spaces and adaptive parameter definition that can be solved using minimum computing requirements in terms of memory and CPU time.

In the following, we introduce the framework developed, examined for segmentation in the torso, as it relates to the study of lung disease. We present the segmentation tools employed, their performance with experimental mouse images, and the consequent integration of the results into a finite-element method (FEM)-based FMT inversion code.

2 Automatic Detection of Anatomical Structures

Automatic detection of specific structures has been of great interest in medical imaging fields. Different approaches have been developed in the last few decades for image segmentation. Typically, the solutions presented work optimally for a particular set of problems and cannot be generalized for any segmentation specification. We consider segmentation of three major structures in the mouse torso, i.e., skeletal tissue, lung, and heart. The image data were taken using a commercial micro-CT[25] with a tube voltage of 80 kV and an electric current of 450 μA. The selection of the torso was driven by an elevated interest to study lung cancer and lung inflammatory diseases such as asthma and COPD associated with pharmacological studies. We found that each tissue required different image processing steps for optimal segmentation, as described in the following.

2.1 *Bone Segmentation*

Since bone structures exhibit high contrast on CT images, they can be easily identified with a conventional application of a threshold, which conveniently is also a fast operation. To automatically assign a threshold, we examined the histogram of the intensities of the CT volume data. When dealing with a normalized scale like the Hounsfield scale, it is straightforward to select a certain threshold that divides the image in bone and background. However, in this work we make no assumption on the CT data scaling so that the method can work seamlessly with different CT acquisition parameters and datasets, since in small animal imaging there exists less standardization between the data obtained, compared to clinical data. The analysis of many histograms of our CT data had shown that there are no significant features representing the intensity of bone tissue, like a local maxima or minima, which could be traced. The intensity of the bones is usually widely distributed throughout the histogram. Therefore we approximated our threshold T_b by finding other distinct intensities, and assume that there is a linear relationship between those intensities and the threshold we need. Mathematically, this can be described by

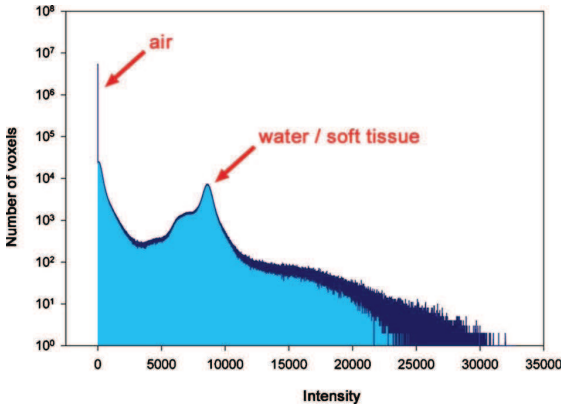

Fig. 1 From the CT volume data, a histogram of the intensities was computed. In this example you can recognize the two distinct peaks (arrows) that represent soft tissue, consisting mostly of water and air.

$$T_b = I_1 + w(|I_1 - I_2|), \tag{1}$$

with I_1 and I_2 being the reference intensity points and w being a factor for weighting the distance between those points.

When considering a typical histogram of a mouse CT, two distinct peaks can be noticed that could be used as reference points (Fig. 1). The highest peak can be found at the left side of the histogram and corresponds to voxels of very low density, in this case primarily the voxels corresponding to the air in the field of view surrounding the animal. A second significant peak, corresponding to water, can also be easily identified as a second maximum in the histogram. Soft tissue contains high amounts of water, and the area around that peak essentially indicates voxels corresponding to soft tissue. These two peaks can be employed for approximating the optimal threshold in Eq. (1). To determine the scaling factor w in Eq. (1), we considered the Hounsfield scale, since it is a common standard for CT images. In the Hounsfield scale, air has an intensity of −1000 Hounsfield units (HU), water has an intensity of 0 HU, and bone structures start at 400 HU, i.e., 0.4 of the water-air difference. Thus in the Hounsfield scale, the threshold for bone structures T_b at 400 HU can be determined by rewriting Eq. (1) as

$$T_b = I_{\text{water}} + 0.4(I_{\text{water}} - I_{\text{air}}), \tag{2}$$

with I_{air} and I_{water} being the intensities of air and water in HU. This equation was utilized to compute the threshold in CT volume data with arbitrary units. The respective peaks representing the intensities of air and water can be determined by simple maxima detection in the according histogram. Using this threshold, the CT images were converted to binary for subsequent processing as described in the following.

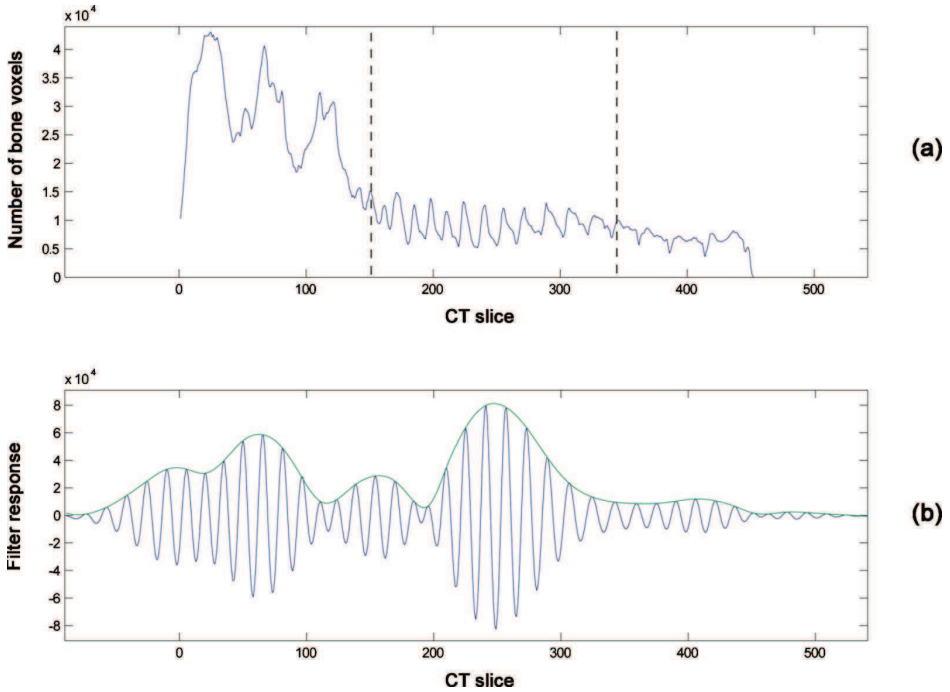

Fig. 2 (a) The histogram function $h_a(t)$ displays the number of segmented bone voxels per slice. Note the very harmonious frequency produced by the ribcage between the dotted lines. The lines mark the beginning and the end of the sternum. (b) The response of the Gabor filter has its highest peak close to the center of the ribcage. The solid line connecting all peaks is the interpolation of all maxima of the filter response.

2.2 *Ribcage Detection*

For segmentation of lung and heart, we considered first the identification of orientation points to serve as initial points for subsequent segmentation steps. In this role, the ribcage serves as an easily identifiable structure that accurately delineates a big part of the outer surfaces of the lung and heart. To identify the ribcage, we analyzed the result of the bone segmentation by computing a histogram of the number of segmented bone voxels per axial slice. We treated the histogram as a signal $h_a(t)$, where t is the slice number. Within this signal the ribcage creates a distinct harmonic frequency [Fig. 2(a)]. To detect the periodicity, we opted for the use of a Gabor filter; essentially a Gaussian function multiplied with a cosine, i.e.,

$$g_{\sigma,\lambda}(t) = \exp\left(-\frac{t^2}{2\sigma^2}\right) \cdot \cos\left(2\pi\frac{t}{\lambda}\right), \tag{3}$$

where the parameters σ and λ define the width and frequency of the filter.

This approach is similar to template matching, where the Gabor function describes the periodic oscillation of the ribcage. Since the frequency of the Gabor filter needs to match the frequency the ribcage produces in $h_a(t)$, specific values for σ and λ had to be defined. To determine those values, we analyzed the frequency produced by the ribcage in three training datasets and adjusted σ and λ so that the Gabor filter fitted this frequency. When performing the ribcage detection on unknown test data, we used the differences of the voxel spacing and voxel size in the training and test data sets to compute a scaling factor for σ and λ. Thus the procedure is independent from scaled image data. Inherent in this procedure is the assumption that the size of the imaged mice does not vary significantly, and that the ribs have a distinct separation to each other. To apply the filter, we convoluted the histogram signal $h_a(t)$ with the Gabor filter $g_{\sigma,\lambda}(t)$. The result of the convolution $h_a(t)^* g_{\sigma,\lambda}(t)$ is a filter response that usually had its global maximum near the axial center of the ribcage [Fig. 2(b)]. Furthermore, we used just the local maxima of the filter response to interpolate a new function [also Fig. 2(b)]. In this function, the next minima to the left and right sides of the global maximum (the center of the ribcage) were selected as landmark points that defined a bounding box in the axial direction around the ribcage. Those landmarks do not necessarily mark specific anatomical points, but usually they appear near the top and bottom endings of the sternum.

To define the bounding box also in sagittal and coronal directions, we computed the histograms $h_s(t)$ and $h_c(t)$ indicative of the number of segmented bone voxels in these directions. Note that we only used the slices between the axial landmark points to compute those histograms. In the histograms, we searched for the global maxima and the first slices left and right to them, where $h_s(t)$ and $h_c(t)$ respectively equal zero, that is, were the ribcage ends. We confined our bounding box only around the ribcage and excluded artifacts outside the mouse that sometimes occur. If this detection scheme experiences difficulties due to noise and artifacts, it is possible to employ searches that define areas where $h_s(t)$ and $h_c(t)$ become smaller than a predetermined value greater than zero to get a bounding box tight around the ribcage. Overall, ribcage determination is an essential step for further detection of ana-

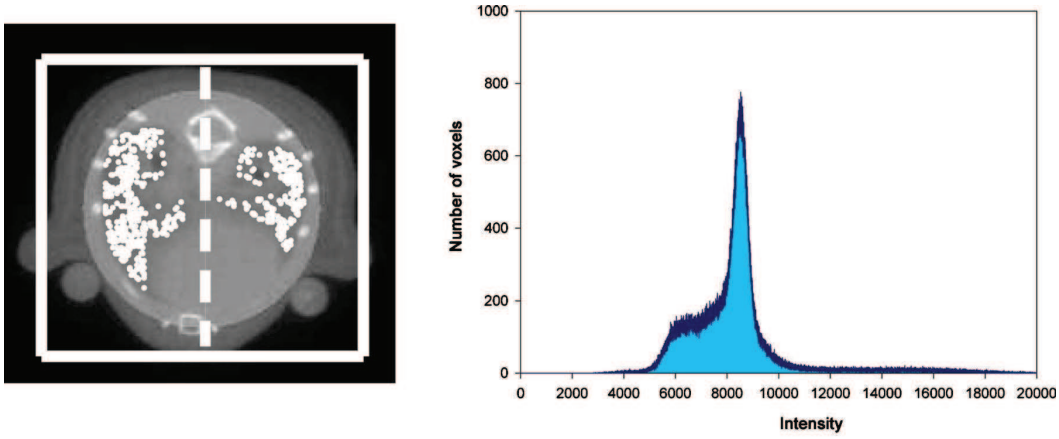

Fig. 3 (a) The image shows a CT slice including the SROI (brighter spherical region), the computed bounding box (solid line), and possible seed points (white spots). The dotted line marks the middle of the bounding box, dividing right and left lobes of the lung. (b) The graph shows the intensity distribution within the region of interest. The peak represents water in the soft tissue.

tomic structures, as described in the following.

2.3 *Lung Segmentation*

To enable lung segmentation, we utilized a seed growing algorithm within the confines of the detected ribcage. For this purpose, possible seed points inside the lungs had to be found automatically. The whole respiratory system can be naturally recognized on XCT images by means of its low density and the corresponding high contrast to surrounding tissue. However, image intensity and contrast alone did not suffice for accurate detection. This was because the bounding box of the seed growing algorithm was usually still wide enough to occasionally contain regions of air outside the mouse or parts of the digestive system that showed also a low intensity and contrast. Other challenges involved the blurring of borders due to possible moving artifacts. To refine the region of interest and achieve a correct segmentation result, we created a spherical region of interest (SROI) inside the bounding box. The SROI was initialized as a sphere with a radius of zero at the center of the bounding box [see Fig. 3(a)], and was allowed to grow so that the sphere radius measured 90% of the distance between the center of the sphere and the boundary of the mouse. In Fig. 3(a) a CT image is displayed with the according bounding box (solid blue line) and the SROI (bright circle).

To find seed points inside the SROI, we computed an intensity histogram from all the voxels inside the SROI [Fig. 3(b)]. Here, the voxels with the lowest intensity I_{low} mark the dark bronchial tubes, and the high peak I_{peak} marks soft tissue. We took these easy to detect points as references to compute an interval $[I_1, I_2]$, where

$$I_1 = \frac{2}{3} I_{\text{low}} + \frac{1}{3} I_{\text{peak}}, \tag{4}$$

and

$$I_2 = I_1 + 0.5(I_{\text{peak}} - I_1), \tag{5}$$

which represents the intensity of voxels that by consequence belong to lung tissue. The parameters of Eqs. (4) and (5) were roughly determined empirically using about five datasets. All voxels of the SROI that possessed this intensity were considered possible seed points for the seed growing algorithm. In Fig. 3(a), these seed point possibilities are marked green.

For the seed growing algorithm itself, a mean intensity $\bar{I}_a$ was defined using the chosen seed point s and its neighboring voxels. Also, a confidence interval was defined by

$$[\bar{I}_a - m\sigma, \bar{I}_a + m\sigma], \tag{6}$$

with σ representing the intensity's standard deviation of the seed point and its neighboring voxels, and m serving as a multiplier to manually control the width of the interval. The algorithm iteratively searched for all voxels that had intensities within the confidence interval and that were connected to the seed point or an already segmented voxel. To avoid oversegmentation, we chose m to be very small. To compensate the resulting undersegmentation, we used multiple, randomly chosen seed points, thereby computing multiple segmentations and combining them. Since the algorithm is sensitive to noise, we smoothed the result by using a Gaussian filter, thereby interpolating small gaps and holes. Finally, we rebinarized the image using a threshold filter.

Because we also wanted to be sure that both the right and left lobes of lung are segmented, we chose an equal number of seed points from both. We distinguished between the right and left lobe by simply dividing our bounding box in the middle.

2.4 *Heart Position Approximation and Segmentation*

The last procedure of our framework is the approximation of the heart position and its segmentation. For this purpose we propose the use of a shape model of the heart generated from

manually segmented training data. In this work we used one manually segmented volume dataset to gain this model. The model is a closed mesh that consists of a number of vertices connected through edges. To yield a rough initial position and scaling factor for the model, we used the bounding box from the ribcage detection as reference. Using the training dataset, we examined the heart position relative to the borders of the bounding box by considering the box as a normalized cube with a side length of 1. We initialized the heart model at the same position in bounding boxes of other CT volume images. A scaling factor for controlling the size of the heart model was approximated using the sizes of the bounding boxes around the ribcages of training and test datasets as references. Scaling factors were computed for all three directions and averaged to get the main scaling factor. This averaging results in a more robust scaling, for our experiments had shown that the sizes of the bounding boxes varied enough to receive unusual heart shapes.

This operation generally placed the heart model close to its supposed position. However, it also attained regions where the heart model was overlapping the other segmentations of the lung and bone structures. This is because of the rough initial position and scale approximation. To adjust the model position, we searched for all of the overlapping voxels and created for each one a unit vector that points to the center of gravity of the heart model. Thus a vector field was created. The field represents forces that push the model away from overlapping sections. After the heart model was translated by the vector field, the procedure was repeated iteratively. A decreasing weighting factor thereby ensures the convergence of the procedure. The iterative process was stopped when either no more voxels with segmentation overlap were detected, or the translational improvement was beneath a specified threshold. The latter usually occurs when there is a balance between forces from opposite sides, i.e., lung and ribcage/sternum, which means that the heart model is too large to fit. We then scaled down the heart model to 95% of its size and restarted the iterative position adjustment until finally no more regions with overlapping segmentations remained.

We note that this algorithm does not provide a segmentation of the heart that fully incorporates wide shape variations. Since the heart model is static, it cannot fully fit the actual image data. Nevertheless, it still can be used as an approximation of a segmentation result and as a new initial position for further, more advanced segmentation algorithms like active contour models that have yet to be implemented.

2.5 *Validation of Segmentation Results*

As a reference for evaluation of segmentation results, we used gold-standard manual segmentation revised by an expert specialized in mouse anatomy. We segmented the whole skeleton, both lobes of the lung, and the heart of a CT volume image with a size of $267 \times 242 \times 452$ voxels on a 64-bit PC with a quad core CPU (2.67 GHz) and 4 GB of RAM. Notice that results of the bone segmentation will always be constant. The lung segmentation algorithm, on the other hand, picks randomly only a few of many possible seed points, thus producing different results. Since the heart position approximation depends on the lung segmentation result, these results vary too. To compensate for this fact, we performed the segmentation process several times to yield the mean performance.

As a main criterion for the evaluation, we used the Dice coefficient $0 \leqslant s \leqslant 1$ with

$$s = \frac{2|X \cap Y|}{|X| + |Y|}, \tag{7}$$

which measures the similarity of two sets X and Y, i.e., the manually and automatically segmented data volumes. Other criteria were the false rejection rate (FRR) and the false acceptance rate (FAR)

$$\mathrm{FRR} = \frac{|X| - |X \cap Y|}{|X|} = 1 - \frac{|X \cap Y|}{|X|}, \tag{8}$$

$$\mathrm{FAR} = \frac{|Y| - |X \cap Y|}{|Y|} = 1 - \frac{|X \cap Y|}{|Y|}. \tag{9}$$

The Dice coefficient is a more general measure for accuracy of the segmentation that the FRR and FAR can also show, if segmentation errors are due to over- or undersegmentation. The FRR measures the amount of voxels of the manually segmented data that were not segmented by the automatic framework (undersegmentation), while the FAR measures the number of voxels of the segmented data that do not belong to the respective tissue (oversegmentation).

3 Fluorescence Molecular Tomography Reconstruction

For fluorescence tomography, the propagation of photons in the tissue was modeled by using the diffusion approximation to the radiative transport equation

$$[-\nabla D \nabla + \mu_a] U_m(r) = -n(r) U_x(r), \tag{10}$$

where D and μ_a are the spatially varying diffusion and absorption coefficients, $n \propto c$ is a function proportional to the fluorochrome concentration c, and U_x and U_m describe the photon density at the excitation and emission wavelength. If D and μ_a are known Green's functions $G(r, r')$, a solution is given by

$$[-\nabla D \nabla + \mu_a] G(r, r') = -\delta(r - r'), \tag{11}$$

leading to

$$U_m(r) = -\int_{r' \in V} G(r, r') n(r') U_x(r') dr'. \tag{12}$$

In addition, to eliminate the influence of varying source intensities and detector sensitivities and to correct for heterogeneous optical coefficients, we used the normalized ratio between fluorescence and transmittance U_m / U_x, as presented by Refs. 31 and 32.

Equation (12) can be inverted by standard methods to yield the concentration measurement n for each voxel r' of the volume data V. Successful inversion requires knowledge of the photon density x, which we modeled by using the same Green's functions as U_m. Green function computations were based on a finite element solution of the diffusion equation.[33]

The finite element mesh was created based on the CT volume data, where the surface of the mouse itself defines the boundary of the mesh. After segmentation, average optical properties representative of the tissue type represented by each node were assigned to the node.

Equation (12) can be transformed into the linear system $Wx=y$ through discretization. Here, W contains the contribution of the integral over G, x is the discretized vector of the concentration values n, and y is the vector of measurements. This equation is usually ill-conditioned and thus a stable solution can be found by minimization of a regularized residual

$$\|Wx-y\|^2+\lambda\|Lx\|^2\rightarrow\min. \tag{13}$$

The anatomical priors from the segmentation procedure were integrated in the regularization term by using Laplace regularization as proposed in Refs. 13 and 15. Here, matrix $\mathbf{L}$ is defined by

$$\mathbf{L}=\begin{bmatrix} l_{1,1} & l_{2,1} & \cdots & l_{w,1} \\ l_{1,2} & l_{2,2} & \ddots & \vdots \\ \vdots & \ddots & \ddots & l_{w,w-1} \\ l_{1,w} & \cdots & l_{w-1,w} & l_{w,w} \end{bmatrix}, \tag{14}$$

where w is the number of voxels in the CT date volume and l is thus given by

$$l_{i,j}=\begin{cases} 1 & \text{if } i=j \\ -\dfrac{1}{w_s} & \text{if voxels } i,j \text{ are part of the same region } s \\ 0 & \text{otherwise} \end{cases}, \tag{15}$$

with w_s being the number of voxels in region s. The regions are defined by the segmentations, thus utilizing spatial information in the reconstruction.

The Laplace prior employed here smoothes estimated fluorochrome distributions within a region while it allows for strong differences across the boundaries of the regions. For comparison to reconstructions without anatomical *a-priori* knowledge, we also used the common Thikonov regularization, with $\mathbf{L}=\mathbf{Id}$, which does not include structural priors.

4 Results

4.1 *Segmentation*

Figure 4 shows the empiric results of the bone segmentation. Notice that very thin bone structures like the blade bones exhibit holes. In our CT images, these structures show lower intensities than bone usually does due to blurring artifacts. Overall, the results yielded Dice coefficients of 0.8721. FRR (0.1062) and FAR (0.1485), which show that these operations resulted in oversegmentation. When we visually evaluated the result, we recognized that nearly all segmentation errors occurred along the borders. This is mainly due to blurring artifacts at the borders between different tissues. Thus we considered these errors to be within normal uncertainty bounds. The segmentation of the bones took 3.3 sec, and the recognition of the ribcage took 1.2 sec, which is very fast for data volumes of such large size.

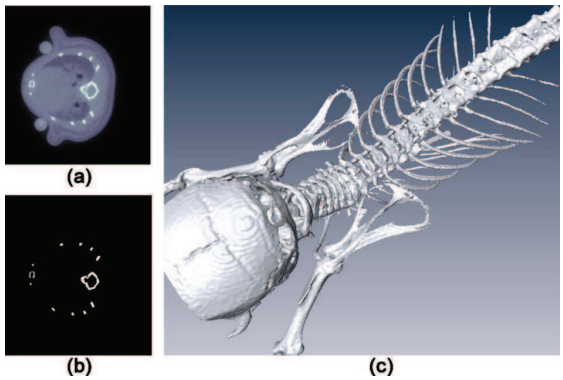

Fig. 4 The result of typical bone segmentation: (a) the original CT slice, (b) the corresponding slice of the segmented data, and (c) surface model of the skeleton computed from the segmentation result.

For the lung segmentation, we analyzed 30 segmentations of our reference image data. We experienced that five seed points per lobe of the lung usually were enough to achieve an accurate and robust segmentation result while still being time efficient. The results are displayed in Fig. 5. The framework achieved a mean Dice coefficient of 0.766 with a variance of 0.007. Nonsegmented voxels (FRR 0.3096) had the greatest influence on this result, while oversegmentation was much smaller (FAR 0.1091). Falsely accepted voxels were usually part of the bronchial tubes outside the lung. The falsely rejected voxels were mostly voxels with a considerably higher intensity, where the lung tissue showed pathologies. The speed of the lung segmentation differs, since the number of iterations of the seed growing algorithm depends on the initial seed point. Usually the segmentation was done in less than 30 sec, including the search for appropriate seed points.

The heart segmentation was also done 30 times. In Fig. 6 you can see the adapted heart model inside the ribcage. The mean Dice coefficient was 0.7647 and had a variance of only 0.0004. Considering that we only used a static model build from one single training dataset, we consider this a very good result. Most notably, this result was due to the quite high FRR

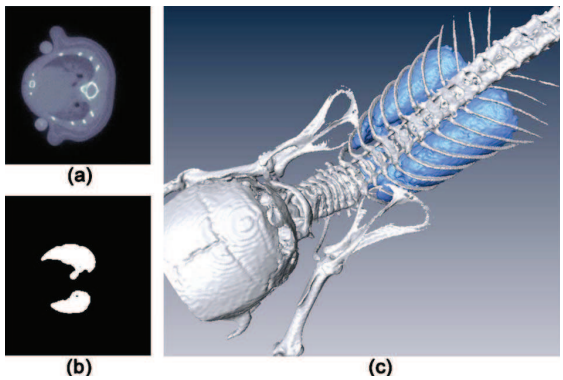

Fig. 5 Result of the lung segmentation: (a) the original CT slice, (b) the corresponding slice of the segmented data, and (c) surface model of the skeleton and the lung computed from the segmentation results.

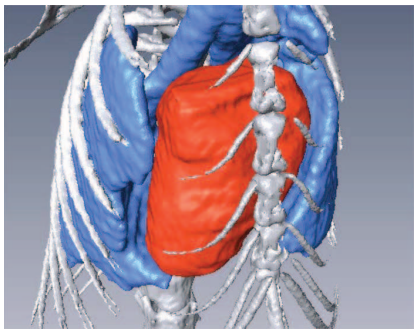

Fig. 6 Result of the heart segmentation. The image shows surface models of all three segmented anatomical structures.

of 0.3378, while only 0.0936 of the segmented voxels were falsely accepted. The time needed for the approximation of the heart also depends on the initial position. On our test data it took less than 45 sec to adjust the heart model.

4.2 *Reconstruction*

Figure 7 shows the results of the utilization of XCT anatomical information as priors in an FMT inversion scheme. The FMT images are laid over the corresponding CT slice. To simplify matters, only one slice out of a reconstructed volume is presented for each approach. For the evaluation of the reconstruction improvement using anatomical priors, we simulated a situation of inflamed lungs [Fig. 7(a)], modeled after previous studies of lung inflammation,[2,34] and used three different reconstruction procedures, i.e., 1. no regularization, 2. inversion using Thikonov regularization, and 3. the Laplace regularization. However, segmentation of the *in-vivo* CT imaging data was done using our framework, and no simulated segmentation was used. We note that the first two approaches do not utilize the segmented information image priors, and that no noise was added in the simulation.

Figure 7(b) shows the inversion obtained without regularization. In this case the inversion generates significant artifacts, especially on the borders leading to a highly inaccurate reconstruction. Figure 7(c) depicts high blurring of the fluorescent signal. The intensity of the signal is also too low, and a prominent spot can be recognized in one lobe of the lung while the intensity should be homogeneous. Finally, Fig. 7(d) shows the best reconstruction results due to the priors. The fluorescence intensity was reconstructed accurately; it is distributed homogeneously in the lung and only small blurring artifacts occur along the borders.

5 Discussion

We have introduced an automatic segmentation scheme for bones, lungs, and the heart for streamlining FMT-XCT inversion. The framework utilized several segmentation and signal processing methods in an automatic manner. Another advantage of the framework is its speed. The segmentation, even in very large volume data, was done in less than 2 min. This renders the approach very useful to integrate it subtly into the FMT reconstruction of our hybrid FMT/XCT imaging system. We proved the quality of the segmentation compared to a gold-standard manual segmentation.

However, the framework still does not exploit its full potential. Most of the parameters of the algorithms were chosen by educated guess and were roughly adapted through examining the measured segmentation quality. We think that optimizing these parameters could improve the segmentation results even more. Most notably there are three parts of the framework that would, in our opinion, benefit from a closer analysis of the parameter values. 1. The computation of a threshold for bone segmentation. Here, the parameter w [Eq. (1)] could be adapted to achieve better bone segmentation. 2. The detection of seed points for lung segmentation. The interval that is used to detect those points could be adapted to yield seed points that are more feasible for the subsequent region growing. 3. The parameters σ and m for the seed growing itself. They heavily influence the algorithm, and we do not know the values to yield optimal results. It should also be considered that the segmentation of the lung and heart depends on the correct detection of the ribcage, and so far the robustness of our approach could not be evaluated. Thus this essential part of the framework should be investigated and improved further. Also, the accuracy of the heart segmentation could be improved significantly. Here, the static, undeformable model proves to be a disadvantage, since it cannot fully adapt to the shape variances. Nevertheless, the approach could be used to initialize more complex segmentation methods such as deformable models that use flexible meshes to overcome this handicap.

We have also shown how the gained anatomical information can be used as *a-priori* knowledge for the reconstruction of FMT images. We proved that this increases FMT image

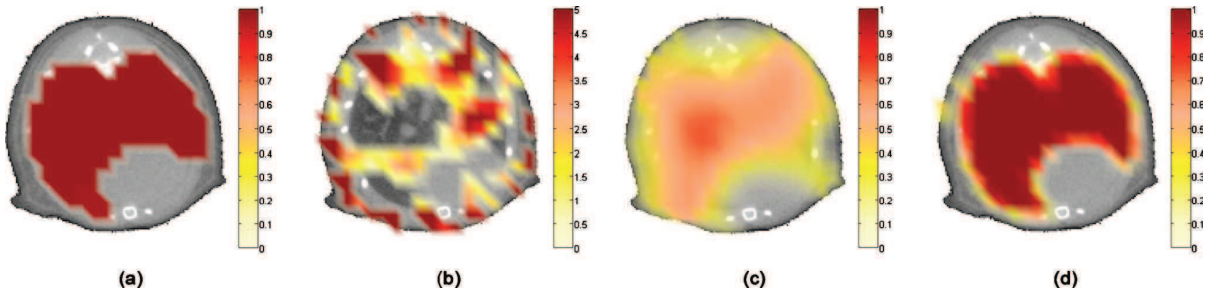

Fig. 7 (a) Simulated fluorescence signal in the lung. (b) Result without regularization. (c) Tikhonov regularization. (d) Laplace regularization showing the best imaging performance in this case.

quality considerably in simulations. Further studies have to be conducted to prove this behavior also for real FMT measurements in *in-vivo* experiments. From our experience, we expect notable FMT image quality improvements in those studies as well. Nevertheless, the conclusion is that we have to put focus on the segmentation of more structures for even better, more accurate FMT reconstruction results. It also has to be discussed how accurate the segmentations need to be, and if more time-consuming and complex segmentation algorithms are actually necessary and practical, because there will always be a tradeoff between speed and accuracy.

Acknowledgments

We acknowledge the help of our laboratory technicians Claudia Mayerhofer and Christoph Drebinger, who cared for our animals and provided much help on our experiments. We also thank Harry Höllig, Peter Hamm, and Thomas Jetzfellner for many fruitful discussions and their precious exterior views to our work that helped us to see some problems from other perspectives. This work was partly funded by the European Commission FP7 FMT-XCT project.

References

1. S. R. Arridge, "Optical tomography in medical imaging," *Inverse Probl.* **15**(2), R41–R93 (1999).
2. V. Ntziachristos, J. Ripoll, L. H. V. Wang, and R. Weissleder, "Looking and listening to light: the evolution of whole-body photonic imaging," *Nat. Biotechnol.* **23**(3), 313–320 (2005).
3. N. Deliolanis, T. Lasser, D. Hyde, A. Soubret, J. Ripoll, and V. Ntziachristos, "Free-space fluorescence molecular tomography utilizing 360 degrees geometry projections," *Opt. Lett.* **32**(4), 382–384 (2007).
4. J. Ripoll, R. B. Schulz, and V. Ntziachristos, "Free-space propagation of diffuse light: theory and experiments," *Phys. Rev. Lett.* **91**(10), 103901 (2003).
5. R. B. Schulz, J. Ripoll, and V. Ntziachristos, "Noncontact optical tomography of turbid media," *Opt. Lett.* **28**(18), 1701–1703 (2003).
6. R. B. Schulz, J. Ripoll, and V. Ntziachristos, "Experimental fluorescence tomography of tissues with noncontact measurements," *IEEE Trans. Med. Imaging* **23**(4), 492–500 (2004).
7. R. B. Schulz, J. Peter, W. Semmler, C. D'Andrea, G. Valentini, and R. Cubeddu, "Comparison of noncontact and fiber-based fluorescence-mediated tomography," *Opt. Lett.* **31**(6), 769–771 (2006).
8. V. A. Markel and J. C. Schotland, "Symmetries, inversion formulas, and image reconstruction for optical tomography," *Phys. Rev. E* **70**(5), 056616 (2004).
9. V. A. Markel and J. C. Schotland, "Multiple projection optical diffusion tomography with plane wave illumination," *Phys. Med. Biol.* **50**(10), 2351–2364 (2005).
10. V. A. Markel and J. C. Schotland, "On the convergence of the Born series in optical tomography with diffuse light," *Inverse Probl.* **23**(4), 1445–1465 (2007).
11. M. Schweiger, S. R. Arridge, O. Dorn, A. Zacharopoulos, and V. Kolehmainen, "Reconstructing absorption and diffusion shape profiles in optical tomography by a level set technique," *Opt. Lett.* **31**(4), 471–473 (2006).
12. S. Srinivasan, B. W. Pogue, H. Dehghani, F. Leblond, and X. Intes, "Data subset algorithm for computationally efficient reconstruction of 3-D spectral imaging in diffuse optical tomography," *Opt. Express* **14**(12), 5394–5410 (2006).
13. S. C. Davis, H. Dehghani, J. Wang, S. Jiang, B. W. Pogue, and K. D. Paulsen, "Image-guided diffuse optical fluorescence tomography implemented with Laplacian-type regularization," *Opt. Express* **15**(7), 4066–4082 (2007).
14. G. Gulsen, O. Birgul, M. B. Unlu, R. Shafiiha, and O. Nalcioglu, "Combined diffuse optical tomography (DOT) and MRI system for cancer imaging in small animals," *Technol. Cancer Res. Treat.* **5**(4), 351–363 (2006).
15. M. Guven, B. Yazici, X. Intes, and B. Chance, "Diffuse optical tomography with a priori anatomical information," *Phys. Med. Biol.* **50**(12), 2837–2858 (2005).
16. A. Li, G. Boverman, Y. H. Zhang, D. Brooks, E. L. Miller, M. E. Kilmer, Q. Zhang, E. M. C. Hillman, and D. A. Boas, "Optimal linear inverse solution with multiple priors in diffuse optical tomography," *Appl. Opt.* **44**(10), 1948–1956 (2007).
17. P. K. Yalavarthy, B. W. Pogue, H. Dehghani, C. M. Carpenter, S. D. Jiang, and K. D. Paulsen, "Structural information within regularization matrices improves near infrared diffuse optical tomography," *Opt. Express* **15**(13), 8043–8058 (2007).
18. C. M. Carpenter, B. W. Pogue, S. D. Jiang, H. Dehghani, X. Wang, K. D. Paulsen, W. A. Wells, J. Forero, C. Kogel, J. B. Weaver, and S. P. Poplack, "Image-guided optical spectroscopy provides molecular-specific information in vivo: MRI-guided spectroscopy of breast cancer hemoglobin, water, and scatterer size," *Opt. Lett.* **32**(8), 933–935 (2007).
19. S. C. Davis, B. W. Pogue, R. Springett, C. Leussler, P. Mazurkewitz, S. B. Tuttle, S. L. Gibbs-Strauss, S. S. Jiang, H. Dehghani, and K. D. Paulsen, "Magnetic resonance-coupled fluorescence tomography scanner for molecular imaging of tissue," *Rev. Sci. Instrum.* **79**(6), 064302 (2008).
20. D. Hyde, R. de Kleine, S. A. MacLaurin, E. Miller, D. H. Brooks, T. Krucker, and V. Ntziachristos, "Hybrid FMT-CT imaging of amyloid-beta plaques in a murine Alzheimer's disease model," *Neuroimage* **44**(4), 1304–1311 (2009).
21. Y. Lin, H. Gao, O. Nalcioglu, and G. Gulsen, "Fluorescence diffuse optical tomography with functional and anatomical a priori information: feasibility study," *Phys. Med. Biol.* **52**(18), 5569–5585 (2007).
22. V. Ntziachristos, X. H. Ma, and B. Chance, "Time-correlated single photon counting imager for simultaneous magnetic resonance and near-infrared mammography," *Rev. Sci. Instrum.* **69**(12), 4221–4233 (1998).
23. V. Ntziachristos, A. G. Yodh, M. Schnall, and B. Chance, "Concurrent MRI and diffuse optical tomography of breast after indocyanine green enhancement," *P. Natl. Acad. Sci. USA* **97**(6), 2767–2772 (2000).
24. B. W. Pogue, H. Q. Zhu, C. Nwaigwe, T. O. McBride, U. L. Osterberg, K. D. Paulsen, and J. F. Dunn, "Hemoglobin imaging with hybrid magnetic resonance and near-infrared diffuse tomography," *Adv. Exp. Med. Biol.* **530**, 215–224 (2003).
25. R. B. Schulz, A. Ale, A. Sarantopoulos, M. Freyer, E. Soehngen, M. Zientkowska, and V. Ntziachristos, "Hybrid system for simultaneous fluorescence and x-ray computed tomography," *IEEE Trans. Med. Imaging* **29**(2), 365–373 (2010).
26. L. M. Gao, D. G. Heath, B. S. Kuszyk, and E. K. Fishman, "Automatic liver segmentation technique for three-dimensional visualisation of CT data," *Radiology* **201**(2), 359–364 (1996).
27. S. Y. Hu, E. A. Hoffman, and J. M. Reinhardt, "Automatic lung segmentation for accurate quantitation of volumetric x-ray CT images," *IEEE Trans. Med. Imaging* **20**(6), 490–498 (2001).
28. J. S. Silva, A. Silva, and S. B. Sousa, "A fast approach to lung segmentation in x-ray CT images," *Proc. 11th Portuguese Conf. Patt. Recog.*, pp. 415–418 (2000).
29. R. Susomboom, D. Raicu, J. Furst, and D. Channin, "Automatic single-organ segmentation in computed tomography images," *Proc. 6th Intl. Conf. Data Mining*, pp. 1081–1086 (2006).
30. C. L. Wyatt, Y. Ge, and D. J. Vining, "Automatic segmentation of the colon for virtual colonoscopy," *Comput. Med. Imaging Graph.* **24**(1), 1–9 (2000).
31. V. Ntziachristos and R. Weissleder, "Experimental three-dimensional fluorescence reconstruction of diffuse media by use of a normalized Born approximation," *Opt. Lett.* **26**(12), 893–895 (2001).
32. A. Soubret, J. Ripoll, and V. Ntziachristos, "Accuracy of fluorescent tomography in the presence of heterogeneities: study of the normalized born ratio," *IEEE Trans. Med. Imaging* **24**(10), 1377–1386 (2005).
33. W. Bangerth, R. Hartmann, and G. Kanschat, "deal.II—a general-purpose object-oriented finite element library," *ACM Trans. Math. Softw.* **50**, 24.21–24 (2007).
34. J. Haller, D. Hyde, N. Deliolanis, R. de Kleine, M. Niedre, and V. Ntziachristos, "Visualization of pulmonary inflammation using non-invasive fluorescence molecular imaging," *J. Appl. Physiol.* **104**(3), 795–802 (2008).

Schrifttumsverzeichnis

Arridge, S.R., Schweiger, M., Hiraoka, M. and Delphy, D.T.A. *Finite Element Approach for Modeling Photon Transport in Tissue*. Med. Phys. 20, 299-309, 1993.

Chalfie, M., Tu, Y., Euskirchen, G., Ward, W.W. and Prasher, D.C. *Green Fluorescent Protein as a Marker for Gene Expression*. Science 1994, 802-805, 1994.

Chance, B. *Optical Method*. Annu. Rev. Biophys. Chem. 20, 1-28, 1991.

Flock, S.T., Patterson, M.S., Wilson, B.C. and Wyman, D.R. *Monte Carlo Modeling of Light Propagation in Highly Scattering Tissues I - Model Predictions and Comparison With Diffusion Theory*. IEEE Transactions on Biomedical Engineering 36, 1162-1168, 1989.

Flock, S.T., Wilson, B.C. and Patterson, M.S. *Monte Carlo Modeling of Light Propagation in Highly Scattering Tissues II - Comparison With Measurements in Phantoms*. IEEE Transactions on Biomedical Engineering 36, 1169-1173, 1989.

Graber, H.L. and Barbour, R.L. *High-resolution Near-infrared (NIR) Imaging of Dense Scattering Media by Diffusion Tomography*. FASEB J. 7, A720-A720, 1993.

Inouye, S. and Tsuji, F.I. *Aequorea Green Fluorescent Protein - Expression of the Gene and Fluorescence Characteristics of the Recombinant Protein*. FEBS Lett. 341, 277-280, 1994.

Joebsis, F.F. *Noninvasive, infrared monitoring of cerebral and myocardial oxygen sufficiency and circulatory paramters*. Science 198, 1264-1267, 1997.

Ntziachristos, V., Ripoll, J., Wang, L.V., Weissleder, R. *Looking and Listening to Light: The Evolution of Whole-body Photonic Imaging*. Nature Biotechnology 23(3), 313-320, 2005.

Prasher, D.C., Eckenrode, V.K., Ward, W.W., Prendergast, F.G. and Cormier, M. J. *Primary Structure of the Aequorea Victoria Green-fluorescent Protein*. Gene 111, 229-233, 1992.

Schotland, J.C. and Leigh, J.S. *Photon Diffusion Imaging*. FASEB J. 6, A446-A446, 1992.